
Article:
Federici, Fabio, Reinke, Matthew L. orcid.org/0000-0003-4413-9613, Lipschultz, Bruce orcid.org/0000-0001-5968-3684 et al. (4 more authors) (2023) Design and implementation of a prototype infrared video bolometer (IRVB) in MAST Upgrade. Review of Scientific Instruments. 033502. ISSN: 0034-6748

https://doi.org/10.1063/5.0128768

Review of Scientific Instruments

Design and implementation of a prototype infrared video bolometer (IRVB) in MAST Upgrade

Cite as: Rev. Sci. Instrum. **94**, 033502 (2023); https://doi.org/10.1063/5.0128768
Submitted: 30 September 2022 • Accepted: 23 January 2023 • Published Online: 01 March 2023
Published open access through an agreement with JISC Collections

Fabio Federici, Matthew L. Reinke, Bruce Lipschultz, et al.

AIP Publishing

Review of Scientific Instruments ARTICLE scitation.org/journal/rsi

Design and implementation of a prototype infrared video bolometer (IRVB) in MAST Upgrade

Cite as: Rev. Sci. Instrum. 94, 033502 (2023); doi: 10.1063/5.0128768
Submitted: 30 September 2022 • Accepted: 23 January 2023 •
Published Online: 1 March 2023

Fabio Federici,[1,2,3,a] Matthew L. Reinke,[2,4] Bruce Lipschultz,[1] Andrew J. Thornton,[3] James R. Harrison,[3] Jack J. Lovell,[2,3] Matthias Bernert,[5] and MAST Upgrade Team[b]

AFFILIATIONS

[1] York Plasma Institute, Department of Physics, University of York, Heslington, York YO10 5DD, United Kingdom
[2] Oak Ridge National Laboratory, Oak Ridge, Tennessee 37831, USA
[3] United Kingdom Atomic Energy Authority, Culham Centre for Fusion Energy, Culham Science Centre, Abingdon, Oxon OX14 3DB, United Kingdom
[4] Commonwealth Fusion Systems, Cambridge, Massachusetts 02139, USA
[5] Max Planck Institute for Plasma Physics, EURATOM Association, D-85748 Garching, Germany

[a] **Author to whom correspondence should be addressed:** fabio.federici@york.ac.uk
[b] See author list of J. Harrison *et al.*, Nucl. Fusion **59**, 112011 (2019).

ABSTRACT

A prototype infrared video bolometer (IRVB) was successfully deployed in the Mega Ampere Spherical Tokamak Upgrade (MAST Upgrade or MAST-U), the first deployment of such a diagnostic in a spherical tokamak. The IRVB was designed to study the radiation around the lower x-point, another first in tokamaks, and has the potential to estimate emissivity profiles with spatial resolution beyond what is achievable with resistive bolometry. The system was fully characterized prior to installation on MAST-U, and the results are summarized here. After installation, it was verified that the actual measurement geometry in the tokamak qualitatively matches the design; this is a particularly difficult process for bolometers and was done using specific features of the plasma itself. The installed IRVB measurements are consistent both with observations from other diagnostics, including magnetic reconstruction, visible light cameras, and resistive bolometry, as well as with the IRVB-designed view. Early results show that with conventional divertor geometry and only intrinsic impurities (for example, C and He), the progression of radiative detachment follows a similar path to that observed for large aspect ratio tokamaks: The peak of the radiation moves along the separatrix from the targets to the x-point and high-field side midplane with a toroidally symmetric structure that can eventually lead to strong effects on the core plasma inside the separatrix.

I. INTRODUCTION

The management of the heat from the fusion reaction is a critical aspect of the design of future tokamak power plants. Of the energy from fusion reactions, about 1/5 is released into the core plasma. When this leaves the core, it is directed to the solid surfaces of the target via a very thin layer of plasma, with a width of the order of a few mm,[1,2] leading to heat fluxes of the order of 10 GW/m^2.[3] Simulations show that to keep the heat flux below engineering limits (of the order of 10 MW/m^2),[4] for ITER, a reduction of a factor of 100 near the separatrix can be achieved thanks to atomic processes, such as excitation/line radiation, charge exchange, and recombination.[5] To further reduce the heat flux detachmenta state in which the plasma recombines in the volume before reaching solid surfaces is expected to be employed.[6] When these conditions are achieved, it is expected that a large fraction of the fusion and auxiliary heating power will be dissipated by the plasma in the form of radiation. The location of the radiating regions can have a significant impact on the core plasma;[7] therefore, it is important to well characterize the power balance and radiated power profile in current machines to understand the stability and performance of strongly radiating plasmas and support predictions for future devices. Key diagnostics

are bolometers that usually operate by exposing a thin foil to plasma radiation and monitoring its temperature. The subject of this paper is a prototype infrared video bolometer (IRVB) installed on the Mega Ampere Spherical Tokamak Upgrade (MAST-U) to study x-point and divertor radiation. The IRVB concept has previously been demonstrated on tokamaks (Alcator C-Mod,[8] HL-2A,[9] JT-60U,[10] KSTAR[11,12]) and stellarators (LHD,[13,14] Heliotron J[15]), and its basic operating principles are well known. A thin foil is exposed to the plasma radiation through a pinhole aperture so that each point of the foil corresponds to a different line of sight (LOS). The foil heats up according to the radiation it receives, and the change in foil temperature is measured via an infrared camera. The advantage, relative to discrete resistive bolometer sensors,[16] lies in the very large number of LOS accessible with a single IRVB device and the capability to image very large or small portions of the plasma based on foil and pinhole relative position. The foil is also a completely passive component, potentially better resistant to neutron irradiation and therefore more reactor relevant than in a resistive bolometer, where on the foil are glued the active resistors used to measure its temperature. The downsides are that the physics of thermal diffusion needs to be considered, which introduces a limit in the time resolution of the diagnostic. The IRVB technique is not new, but the current application in MAST-U represents the first successful implementation on a spherical tokamak. Additionally, in most cases, the IRVB is tuned to image the core plasma, while in this case the aim is to measure the radiated power profile in the vicinity of the lower x-point with high resolution. This choice also comes from the need to complement the MAST-U resistive bolometry system with a radiated power diagnostic with high resolution in a region of the plasma characterized by sharp variations. This paper will detail the considerations that dictated this prototype design. The entire calibration procedure and the lessons learned from this implementation will also be presented. Early results from the first experimental campaign in MAST-U (MU01) will be shown.

II. IRVB BASICS

A sketch of the IRVB in MAST-U is in Fig. 1.

There are various elements to consider in the design of the IRVB diagnostic, as shown in Fig. 1. Considering how thin a typical carbon coated foil is (composed of 10 μm graphite + 2.5 μm platinum + 10 μm graphite as per[17] their standard properties), when the temperature on one side is increased by a set amount, it takes ~7 ns for the other side to reach 99% of that increase. The heat transfer across the foil is so fast compared to the maximum frame rate of the infrared (IR) cameras available (10 kHz) and the timescale of the phenomena of interest (1–10 ms) that it permits treating heat diffusion as a 2D problem. The thinner the foil, the lower the thermal inertia, allowing for a higher temperature rise for a given input power. The thickness must nevertheless be large enough for the vast majority of the radiation to be absorbed. The foil must also (if a significant amount of neutrons are produced by the plasma) be made of a material weakly prone to neutron induced transmutation and vacuum compatible.[18] It is important that the foil has low reflectivity for the wavelength range of interest. Metals normally used in bolometers have low reflectivity for UV and shorter wavelengths but high for longer as the majority of radiation from the plasma is emitted at VUV wavelengths. This is usually addressed by coating the foil with a thin layer of carbon (as done in our case), known as "blackening," that weakly absorbs and reflects high-energy photons but has low reflectivity and high absorption at low energies. The coating does not significantly impact the reflectivity of radiation entering the diagnostic at shallow angles and reaching the foil supports.[19] This light would require multiple reflections to reach the foil and would, therefore, be scattered, resulting in a weak offset over a large portion of the foil. This would not change its capability to observe sharp features in the plasma. The coating introduces an interface between materials that might impede heat transfer and increases the mass of the foil, increasing its inertia. The coating could also, depending on the technique, be deposited non-uniformly on the foil, adding to the non-uniformity already present on the foil. The coating must also be stable and vacuum compatible.[20]

The infrared camera must be positioned as close as possible to the foil in order to increase the resolution and signal-to-noise ratio. If the neutron flux is significant or there are mechanical constraints, mirrors or periscopes must be used. All apparatus must be suitable to transmit infrared radiation and properly coated to avoid reflections. The camera itself has to be suitable for measuring temperature differences of a few K around room temperature or vacuum vessel temperature. Of great importance in the design is the positioning and size of the pinhole aperture with respect to the foil. The distance and position impact the field of view (FOV) of the diagnostic, its spatial resolution, and the radiation intensity.

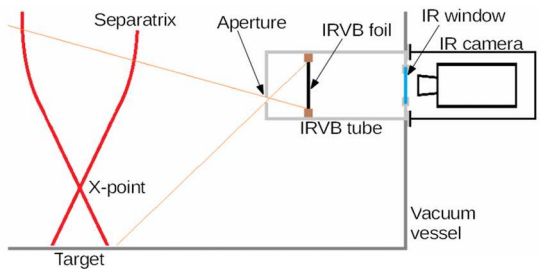

FIG. 1. Schematic representation of the main components of an IRVB diagnostic.

III. MAST-U IRVB DESIGN

The IRVB design is based on work previously done for NSTX-U,[21] and here it will be shown how the design was adapted to the specific geometry of MAST-U. The vertical location of the IRVB was dictated by the available ports on the machine. The one assigned to the IRVB is HE11-2, located in sector 11 and centered 0.7 m below the midplane. The pinhole was placed as close as possible to the plasma to enable an unobstructed, wide field of view while being protected by the surrounding structures and safely outside the plasma scrape-off layer (SOL), at a radius of 1.55 m. The resulting positioning of the IRVB tube can be seen in Fig. 2.

With the above constraints, the pinhole was located off the center of the foil so that the LOS starting from the x-point in the poloidal view of the plasma would land in the center of the foil. Two-thirds of the foil surface will have a mostly poloidal view of the plasma, while one-third will have a mainly tangential view. The foil is com-

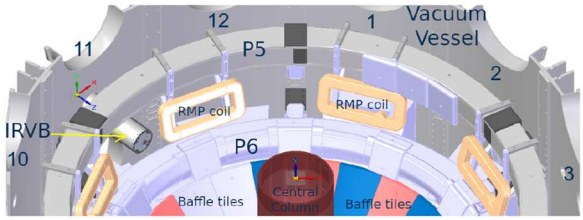

FIG. 2. Top view of the lower half of MAST-U, showing the positioning of the IRVB inside the vacuum vessel with respect to other features. The numbers identify the sectors, assigned clockwise in the toroidal direction.

posed of a 2.5 μm platinum film coated with graphite on both sides with dimensions 9×7 cm^2 as supplied by the National Institute for Fusion Science (NIFS), with the longer side aligned with the vertical axis of the machine to provide large coverage in that direction. An exploded view of the components and their final appearance is shown in Figs. 3 and 4 respectively. In the design of the assembly, particular care was dedicated to:

1. The presence on the re-entrant and air side section of the diagnostic of features that can be used to align the view with the MAST-U geometry as intended.
2. The mechanical rigidity of the assembly and the increase in magnetic permeability due to welds. The tube has a weld along its length that was heat treated to reduce the relative magnetic permeability below 1.05.
3. Blackening all the surfaces that could cause reflections and direct light to the foil. The entire detector sub-assembly was blackened with Moly-Paul powder in an isopropanol solution [the same used within the MAST-U vacuum vessel (VV)], while it was deemed sufficient to grit blast the other surfaces.
4. The presence of cutouts in the tube to equalize the pressure within. The effect of rapid pressure changes was tested on a dummy foil created for this purpose in the benchtop setup (see Fig. 15), causing no motion of the foil with depressurization of up to 0.05 bar/s (only cooling due to ambient air decompression) and visible motion but no damage up to 0.2 bar/s.

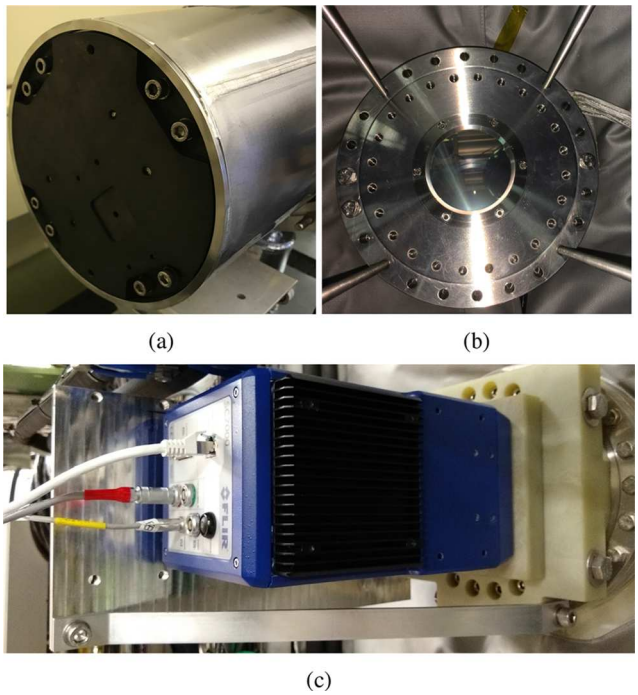

FIG. 4. IRVB components overview: (a) photograph of the foil assembly inside the tube, (b) the view port side of the tube installed in MAST-U, and (c) the camera installed on the flange, respectively. Photographs taken on July 23, 2018, December 03, 2018, and May 14, 2021, respectively. To change pinhole size and foil pinhole distance, the tube must be removed while the camera is always accessible.

5. Maintaining electrical isolation between the tube and the absorber assembly (foil and copper plates) with PEEK isolation washers to avoid eddy currents through the absorber.
6. Use of vented screws for tapped holes to avoid trapping air and slowing down the vessel pump down.

The power density on the foil was estimated with CHERAB,[22–24] a code that can perform ray tracing with the full geometry of MAST-U. Based on prior experience with the IRVB

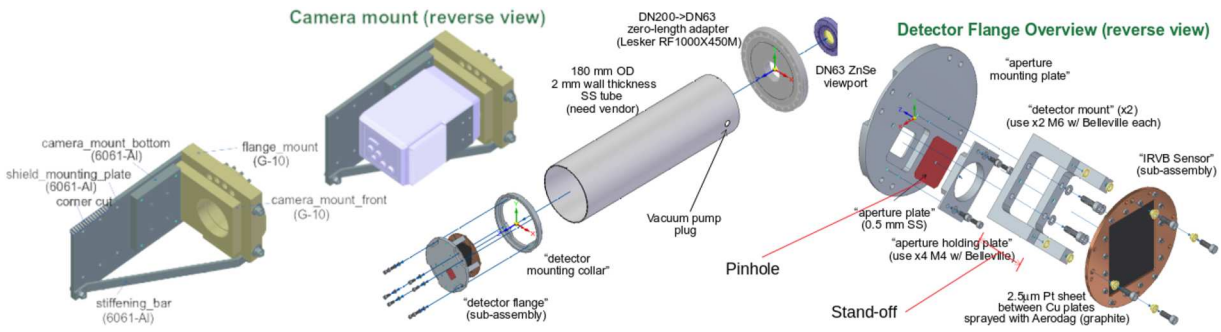

FIG. 3. IRVB components overview: an exploded view showing all internal components before welding and assembly.

on the NSTX-U,[25] the noise equivalent power density (NEPD) is expected to be in the region of ~5 W/m^2, and so a desired signal of ~100 W/m^2 was utilized in the pinhole camera design.

The power distribution on the foil was also simulated in the case of a core and divertor region filled with a homogeneous emitter.[26] See Fig. 5.

The bottom left region of the image is where no radiation can arrive. This could have been helpful for the prototype phase because that area could have been used as a reference where the power is zero. For this reason, it has been decided to adopt a stand-off between pinhole and foil distance of 45 mm for MU01, which covers the results shown in this manuscript. This allows for intense enough radiation from the X-point to adopt a relatively small 4 mm diameter pinhole, allowing for better resolution. In Fig. 6, it is illustrated how, with a smaller pinhole, the signal level is lower but it is easier to identify close but distinct structures in the radiation distribution, even from the poloidal view alone (the left side of the foil). For closer radiating structures, it would be easier to distinguish them as separate in the tangential view (right side of the foil) with a smaller rather than large pinhole. The MAST-U IRVB diagnostic has been returned to operation on MAST-U for the second campaign (MU02) with a stand-off of 60 mm, which enables higher spatial resolution within the divertor region.

An approximate view inside MAST-U, imagining that the IRVB operates as a camera to show the features and obstructions, is shown in Fig. 7. The view of the plasma is mainly poloidal on the left side of the central column, but the field of view is large enough to see both sides of the central column.

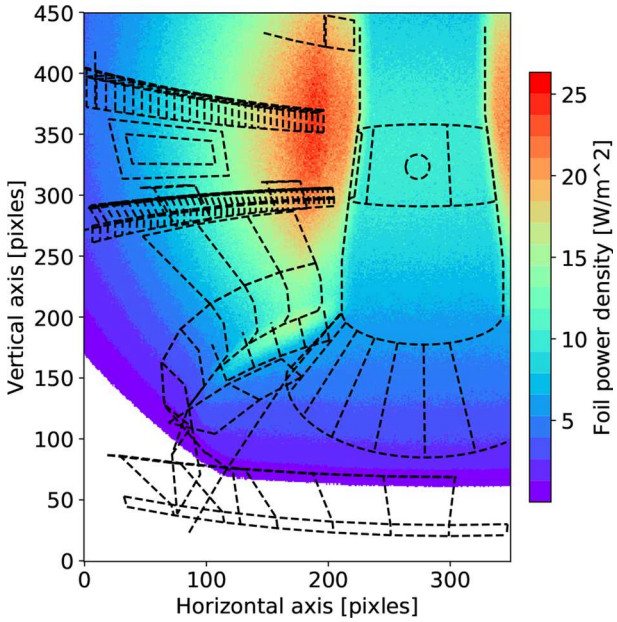

FIG. 5. Radiated power deposited on foil with a 4 mm diameter pinhole and a 45 mm stand-off between the pinhole and foil in the case of the core and divertor regions emitting homogeneously at a level of 50 kW/m^3. The white region does not receive any radiation from the plasma, in black are overlaid the projections of the relevant features of the MAST-U structure on the foil for reference.

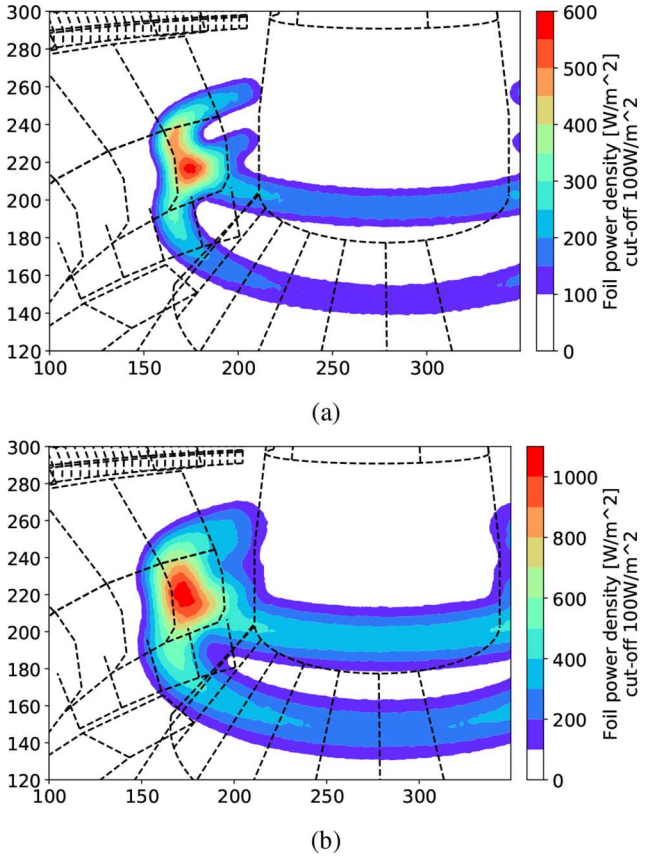

FIG. 6. Radiated power deposited on foil, modeled with CHERAB, from two toruses of 4 cm minor radius separated by 16 cm in vertical position with uniform emissivity such as to total 0.5 MW of radiated power, located at the expected x-point location. The pinhole size was varied from 4 mm (a) to 6 mm (b) to illustrate the loss of spatial resolution. The power deposited on the foil below 100 W/m^2 is not shown, as that is the minimum desired signal level. Only the relevant section of the foil is shown. In black are overlaid the projections of relevant features of the MAST-U structure on the foil for reference.

Figure 8 displays the overlap between the coverage and views of the resistive bolometry system and those of the IRVB. The core resistive bolometer LOSs are mostly suited to measure the fairly homogeneous core emissivity profiles on a flux surface, as there is no overlap between the various LOS. The super-x chamber has good coverage, but only between the x-point and the entrance to the divertor, defined by the baffle. The IRVB is aimed at filling the gap between the two systems.

The assembly holding the foil is composed of a 2.5 μm thick platinum foil from Nilaco, Japan, held between oxygen-free copper plates, and was originally prepared by NIFS. The foil is the same as that used in Alcator C-mod,[8] where it is described in more detail. The foil thickness is optimized to stop photons with energies up to 8.2 keV.[14,19] The foil and its support frame have been spray-blackened on both sides with Aerodag® G Graphite Aerosol and calibrated with a procedure analogous to the one described in Ref. 28. The layer of graphite helps to absorb radiation in the visible range, avoiding reflection; even if its thickness is larger than

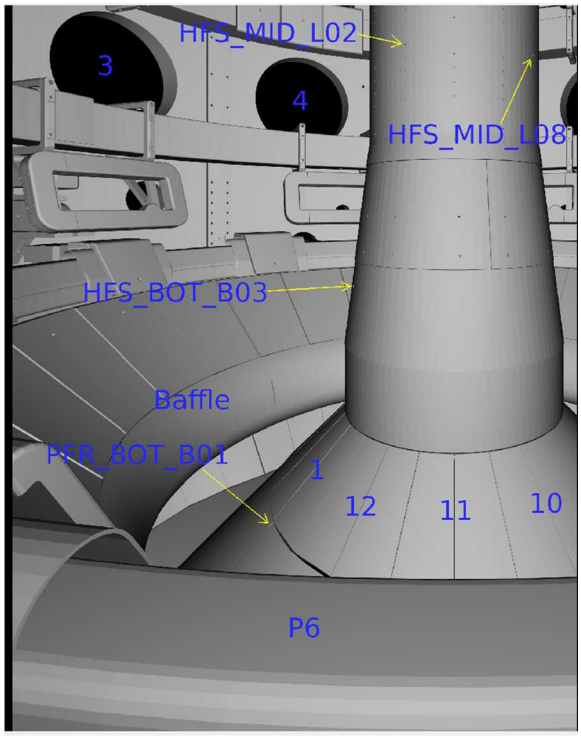

FIG. 7. Approximate view inside MAST-U as if the IRVB operated as a camera. Blue labeling is used to highlight the various sectors and the fueling locations in the IRVB field of view (FOV). At the bottom of the image is the coil P6 obstructing the field of view.

the platinum layer,[17] it should be thermally irrelevant.[29] Lower-energy photons, such as visible light, represent a minor energy loss channel, but their relevance is expected to increase in deeply detached and cold plasmas, therefore, the importance of the coating.[30] In Ref. 20 it is shown that this type of coating causes irregularities in the foil, leading to non-uniform temperature increases. To alleviate this issue, the carbon layer can be deposited with a vacuum evaporation technique that guarantees reproducibility and uniformity, as done at LHD.[20] Given the prototype nature of the present implementation and the availability of a vacuum-compatible certified absorber, this foil was deemed sufficient.

To guarantee consistency in the positioning and orientation of the foil with respect to the pinhole, a series of markings were inscribed by NIFS on the copper plates as shown in Fig. 9. The yellow numerical markings are also used to define the thermal calibration supplied with the foil. The compatibility of the assembly with the thermal expansion caused by the MAST-U VV bake was studied. The bake causes the VV and internal components to reach ~110 and 120–200 °C, respectively, likely causing the absorber assembly to reach an intermediate temperature. The thermal expansion coefficients for Cu and Pt are 16 μm/mK (similar to steel) and 9 μm/mK, respectively. This could have led to stress and thus tearing of the foil, but confidence was gained with the pressure test mentioned in Sec. III on the mechanical resilience of the foil. Another item of concern related to the bake is the stability of the carbon coating on the absorber foil. The technical datasheet for Aerodag

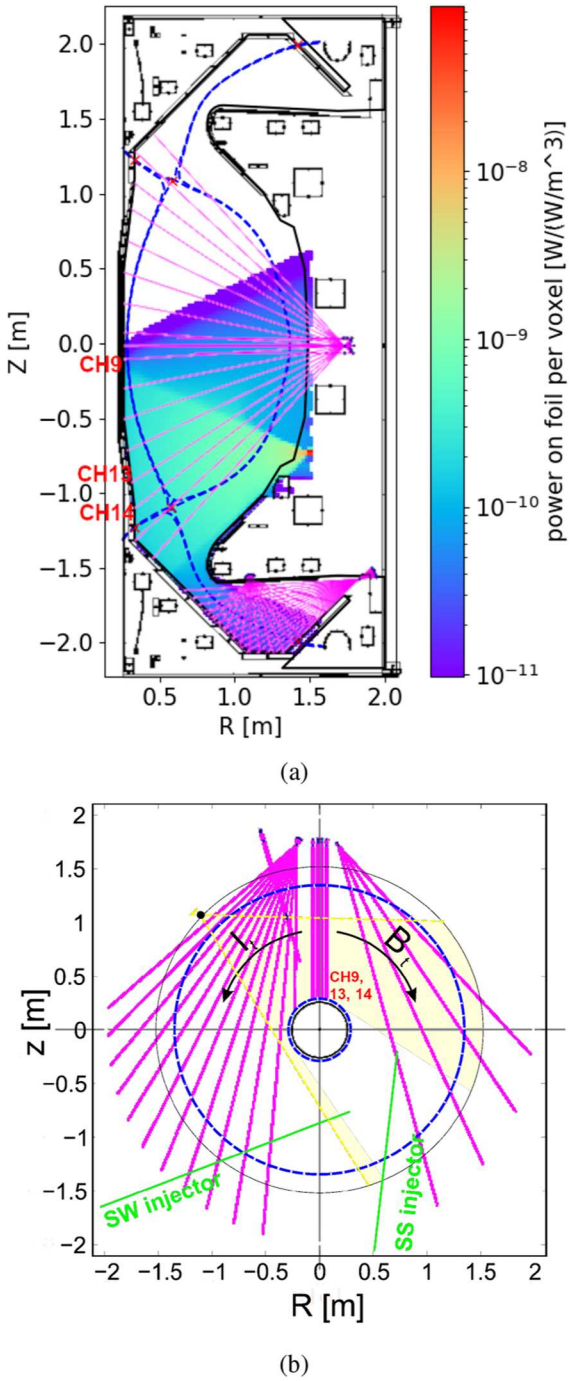

FIG. 8. (a) Poloidal view of MAST-U showing the comparison of the resistive bolometer system LOS (magenta) with a color plot obtained by scanning all the voxels with a 1 W/m^3 emitter and integrating the power absorbed by the foil, indicating the regions of higher sensitivity of the IRVB. (b) Top view of MAST-U showing the positions of the neutral beam injectors (NBI, green), the co- and counter-NBI resistive bolometer LOSs, and the IRVB FOV (yellow, mostly counter-NBI). Adapted from Ref. 27. For reference, the separatrix of a typical plasma is shown as an overlay of a blue dashed line. The resistive bolometer LOSs that will be used in the later analysis are identified here.

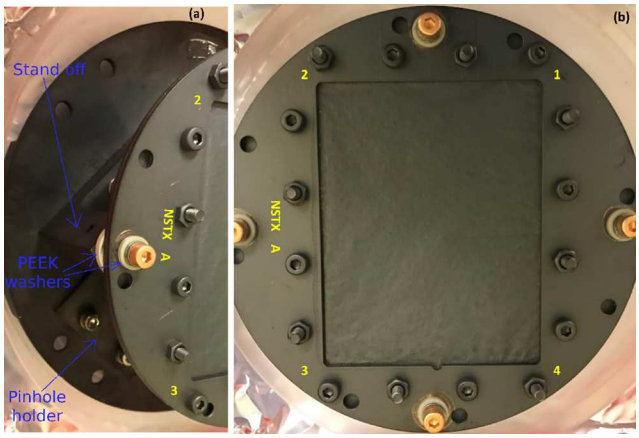

FIG. 9. Photographs of the foil in relation to the pinhole (a) and of all the identifying markings (b), taken July 23, 2018.

G used for coating indicates that it can be used as a lubricant up to 200 °C. Considering the possible failure modes, any piece of carbon detaching from the absorber assembly was expected to stay within the tube, posing no risk for MAST-U operations. The IRVB ultimately underwent the entire bake cycle prior to MU01 and, after inspection, did not seem to suffer any damage.

The tube where the foil is installed extends from the vacuum chamber wall to a position close to the plasma but still safely outside the SOL and potential particle and power loads. The camera images the absorber foil through a 10 mm thick ZnS view port from Crystran with a 4–5 and 8–10 μm anti-reflection coating on both sides and is bolted to the tube. The orientation of the view port with respect to the camera, even if it should not matter substantially, was maintained throughout the test and assembly phases for consistency. The view port assembly was leak checked before final installation with the setup in Fig. 15. The camera, a FLIR SC7500 with an InSb detector array, is equipped with a 4–5 μm pass band filter and has a spectral range of 1.5–5.1 μm. This model was selected so that the same could be adopted for other diagnostics in MAST-U and the same acquisition software could potentially be developed. This is inconvenient for the IRVB, as the optimal wavelength for a black body radiator around room temperature is around 10–14 μm. Considering that the volume between the foil and camera is fully enclosed in the IRVB tube and that the temperature of the entire assembly does not deviate appreciably from room temperature during the short duration of the pulse, the use of the filter would not have prevented any stray light from affecting the measurements. For this reason, the camera was used without the internal filter, increasing the signal. At the maximum frame rate at full frame (383 Hz) and 2 ms integration time, a strong signal around 11 000 counts is measured (see Fig. 13), with saturation at 2^{14} = 16 384 counts and a noise floor ~5 counts. During testing, a design flaw in the present IRVB design was discovered. It became clear that, even with the presence of the anti-reflection coating, the view port caused the so-called "narcissus effect." This happens when the camera can see its own reflection on the view port, hence "narcissus." The view is orthogonal to the camera FOV, so at its center is the image of the reflection of the sensor array. The detector array is cooled to about −203 °C, while around it the body of the camera is slightly above room temperature. This causes a "dark spot" to appear at the center of the image. The main difficulty in dealing with the effect arises from the inability to perfectly match the orientation of the view port during calibration and on the machine. Ultimately, this systematic error, if stable intra-shot, does not affect the temporal and spatial temperature derivatives on which the analysis primarily relies. In future iterations of the diagnostic, the view port should be angled with respect to the camera so as to reflect light from an area with a more homogeneous temperature and emissivity.

The camera is bolted to aluminum plates cantilevered off an insulating G-10 piece that is connected directly to the vacuum vessel flange (to stop induced current loops), as shown in Fig. 4. The aluminum plates holding the camera have multiple holes so that the camera can be located at four fixed distances from the view port (8.7, 11.2, 13.7, and 16.2 cm), with the closest being the one with the foil in focus. The ability to vary the camera location allowed us to progressively test the compatibility of the camera with a magnetic field. That data were collected during the commissioning phase of the MAST-U magnets while the camera was first as far as possible from the VV. Once the maximum field was reached, the camera was then progressively moved toward its final position while checking that no anomalies in its operation arose. The camera operated normally at all distances, making a magnetic shield around it unnecessary.

IV. SYSTEM CALIBRATION

Before scientific utilization, the IRVB diagnostic has to be properly calibrated. This includes the temperature response of the IR camera, the thermal response of the foil, and the spatial alignment of the pinhole and camera. Laboratory tests can be performed for the first two calibrations, while the third was verified during operation using observed features inside the tokamak.

A. Counts to temperature model

The temperature calibration is the procedure used to convert the camera raw data from counts to temperatures. It involves defining the mathematical model for the conversion and finding the coefficients required. Once defined, it can be applied to MAST-U data to obtain the IRVB foil temperature. The surface of the foil is approximated as a black body emitter. The total number of photons emitted by a BB source Φ_p within the camera integration time can be modeled as per the following equation:

$$\Phi_p(T) = \varepsilon i \int_{\lambda_1}^{\lambda_2} \frac{2\pi c}{\lambda^4} \frac{1}{e^{\frac{hc}{\lambda kT}} - 1} d\lambda, \tag{1}$$

where ε is the emissivity, i is the integration time, λ is the wavelength, $\lambda_1 - \lambda_2$ is the wavelength range allowed by the camera or filter, and T is the surface temperature. To simplify the calculations, an interpolator is built such that

$$\frac{\Phi_p(T)}{T} = \alpha(T), \quad T = \alpha_r(\Phi_p). \tag{2}$$

The number of photons reaching the camera is proportional to the number of photons emitted from the absorber foil (a_1), with

an additional offset due to thermal photons originating from the view port and the air between the sample and camera as well as their reflections (a_2). This offset will be approximately constant because it will not depend on the surface temperature observed by the camera. Assuming that the number of counts is proportional to the number of photons and that this does not depend on the photon wavelength, the number of camera counts can be expressed as

$$C = a_1 \cdot \Phi_p(T) + a_2, \tag{3}$$

where $a_1 \in [0, \infty]$ and $a_2 \in [-\infty, \infty]$ the proportional and constant components. Once a_1 is determined, the temperature is calculated as

$$T = \alpha_r(\Phi_p(T)) = \alpha_r\left(\frac{C - a_2}{a_1}\right) = \alpha_r\left(\frac{C - C_0}{a_1} + \Phi_p(T_0)\right). \tag{4}$$

T_0 and C_0 are the temperatures and counts relative to the initial conditions at the beginning of the shot (approximated with the vacuum vessel temperature). The power absorbed by the IRVB foil is obtained using the temperature increase over the profile before the pulse, so the constant offset from the calibration will not impact the results.

B. Temperature calibration

Given that the IRVB relies on measuring small temperature differentials with high precision, it was necessary to calibrate all camera pixels independently. Given that a black body source that could encompass the entire field of view with the image in focus was not available, the method employed was similar to the one by Reinke.[8] A Sofradir non-uniformity correction (NUC) plate, built such that it emits black body radiation uniformly with an emissivity close to 1, was used. The plate was then heated in an oven to ~70 °C, then left to cool to room temperature while taking samples with the IR camera. Similarly, the plate was also cooled below room temperature and observed while heating up. The temperature of the plate was monitored with a thermocouple. For consistency, two cooling and heating temperature ramps were performed, and the data fitted with the model in Sec. IV A. The infrared camera is equipped with two distinct digitizers; therefore, the calibration will be operated independently for each. This means that the two digitizers behave as two distinct instruments; the power absorbed by the foil will be calculated independently for each and then averaged, causing a reduction of the maximum (full frame) frame rate from 383 to 192 Hz.

The geometry of the calibration is represented in Fig. 10. The relative distances are the same as when the camera is installed. The rotational orientation of the view port was maintained during calibration and on the machine thanks to markings on the side of the window. During testing, the narcissus effect was clearly observed.

Figure 11 displays the qualitative effect of the presence of the view port. Figure 11(a) shows the typical view when the camera images the NUC plate; vignetting due to the camera lenses is apparent. Figure 11(b) shows the effect of the window reflections. In Fig. 11(c) the effect on the foil image is shown. The dark spot caused by the narcissus is at the center of the image, decreasing the counts by ~200 counts at an integration time of 2 ms. This should be a systematic error and, therefore, mostly impact the a_2 coefficient, which ultimately doesn't impact the temperature measurement. During the temperature ramps, it was observed that the NUC plate, despite having a uniform emissivity, showed a non-uniform temperature across the FOV due to heat transfer. The plate is naturally cooled/heated via conduction, convection, and black body radiation. Air flows around the plate and can lead to uneven heat transport.

The temperature non-uniformity across the image was estimated for different temperature ramps, as shown in Fig. 12(b), and it was found to be at most 0.3 °C on average in the temperature range of interest. As shown in Fig. 12(a), the spatial variation of temperature is very slow, with a very minor impact on the spatial and temporal derivatives. The effect of the location where the thermocouple is connected to the NUC plate was also investigated by moving it to different corners of the plate. The spread of the temperature around a curve that fits average camera counts and temperatures for all the probe positions with the model in Sec. IV A is about 0.25 °C. There was, though, no pattern found, so the difference is most likely due to the connection of the sensor to the plate rather than the actual temperature of the plate.

The result of the scan for the two pixels identified in Fig. 11, one close to the center of the narcissus effect and one on its side, is shown in Fig. 13. Equation (3) can reproduce the measurements with high accuracy. As expected, the presence of the narcissus mostly affects the a_2 offset.

The results of the calibration for the entire foil are shown in Fig. 14. Both coefficients are affected by vignetting and the narcissus effect. It is noteworthy that the ~200 counts at the center of

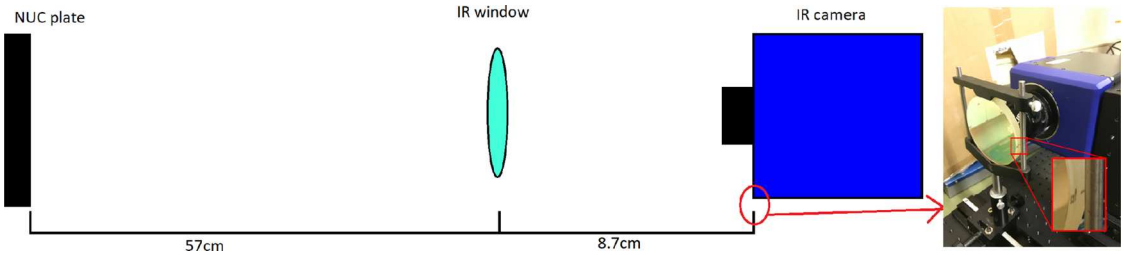

FIG. 10. Schematic of the calibration setup. The NUC plate and the IR window are located at the same distance from the camera as when installed and as per design. Effort is made to keep the window in the same rotational orientation. See the marking for the view port alignment in the detail.

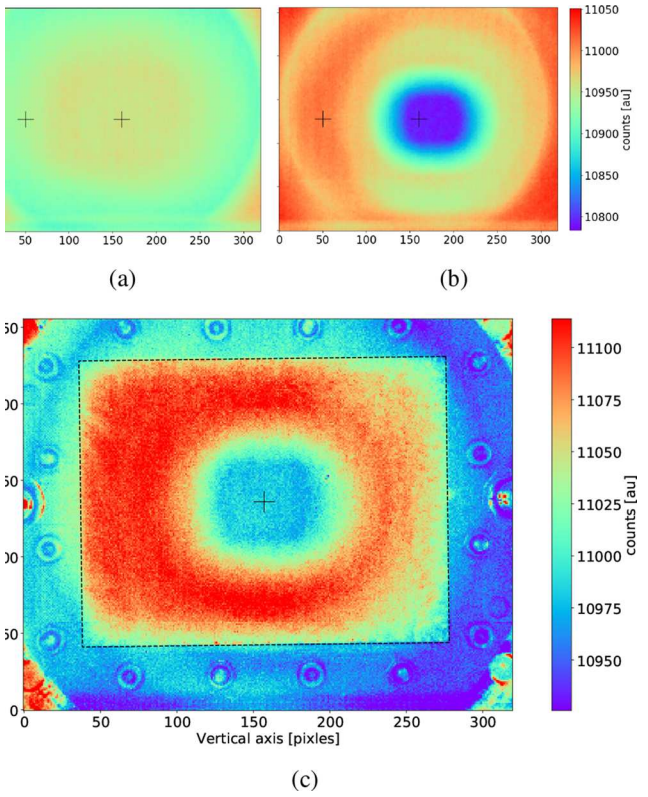

FIG. 11. Example of non-uniformity of the counts of the IR camera when aimed at the NUC plate at room temperature. Shown are the images without the view port (a) and with (b). The same scale is applied to both plots, and there was a 2 ms integration time. The black cross indicates two reference points (inside/outside the narcissus) that will be used in later analysis. (c) shows the position of the foil (the red square) inside the camera field of view. Around the foil are the bolts that lock the foil in between the two copper plates, which can be used to identify the foil orientation.

the narcissus are assigned entirely to the constant parameter, as one would expect for a systematic error. Some of the variation in a_1, especially the red ring around the center, could be related to the narcissus, meaning that its effect is not completely independent of temperature. The variation in a_1 is very small, howeveronly ~2% and changes fairly slowly across the FOV, resulting in a small impact on the spatial and temporal temperature derivatives. Both coefficients seem to have a general dependency on the vertical direction (right to left in the figure), possibly due to the slight non-uniformity of the temperature of the NUC plate.

For future calibrations, a large flat black body calibration source with the capability to cool below and heat above room temperature could be used to further reduce the uncertainties in the NUC plate temperature.

C. Foil model

The foil thermal response is dictated by heat transport: the source is the radiated power from the plasma (P_{foil}), while the local sinks are its black body radiation (P_{BB}), conduction ($P_{\Delta T}$), and temperature variation ($P_{\frac{\partial T}{\partial t}}$). The foil is very thin, and therefore 2D heat transport can safely be considered instead of 3D. Equation (5) shows how to calculate the power absorbed by the foil based on its temperature.

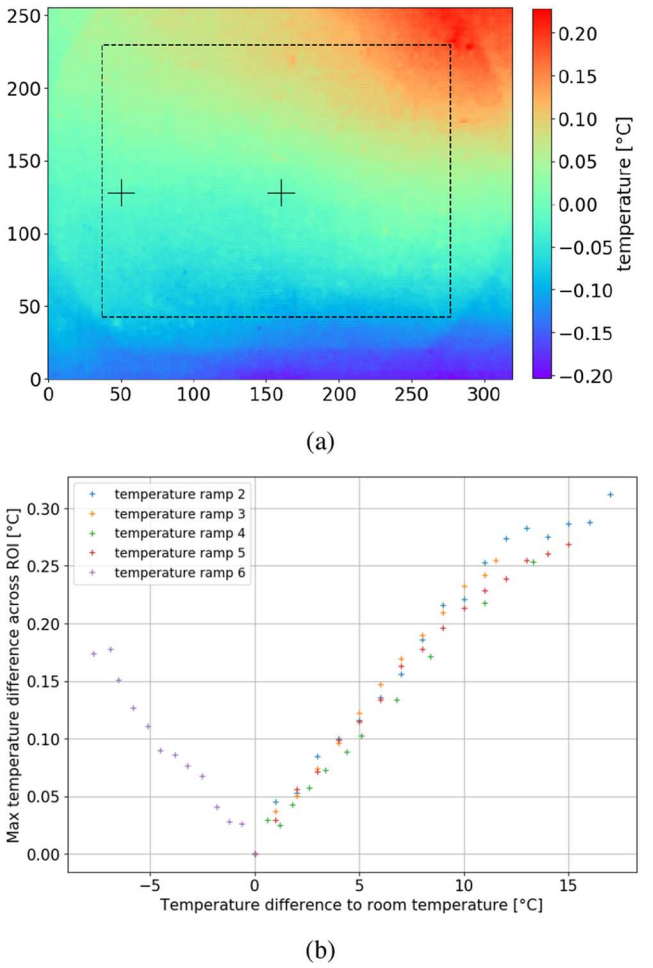

FIG. 12. (a) Shown are the IR camera counts at 41.9 °C minus the counts at room temperature, scaled up such that the average across the foil is the same as at high temperature. In black is highlighted the region corresponding approximately to the IRVB foil and the two reference points defined in Fig. 11. The vertical orientation is bottom to top here, with the top of the image being up. (b) Peak temperature difference between the temperature deriving from the counts at high temperature and the counts at room temperature, scaled up as previously mentioned.

$$
\begin{aligned}
P_{foil} &= P_{\frac{\partial T}{\partial t}} + P_{\Delta T} + P_{BB},\\
P_{\frac{\partial T}{\partial t}} &= \frac{k\, t_f}{\kappa}\frac{dT}{dt},\\
P_{\Delta T} &= -k\, t_f \left(\frac{\partial^2 T}{\partial x^2} + \frac{\partial^2 T}{\partial y^2}\right) \approx -k\, t_f\, L \cdot T,\\
P_{BB} &= 2\,\varepsilon\,\sigma_{SB}\,(T^4 - T_0^4),
\end{aligned}
\tag{5}
$$

where k is the thermal conductivity, t_f is the thickness, κ is the thermal diffusivity, ε is the black body emissivity, and σ_{SB}

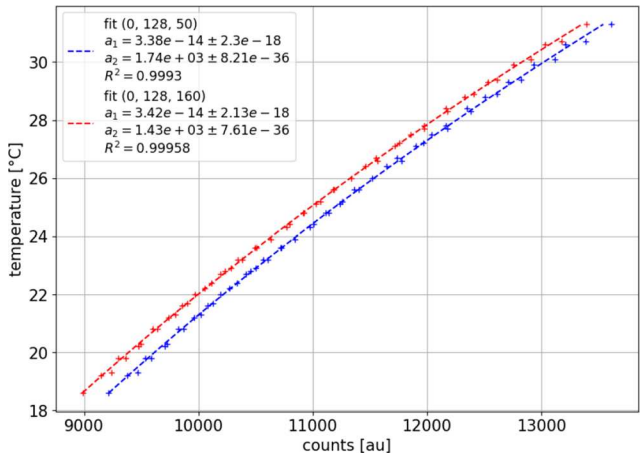

FIG. 13. Comparison of the temperature calibration curves for a pixel at the center of the narcissus (red) with one on its side (blue). The legend gives the fit parameters (a_1 proportional and a_2 additive components), their uncertainties, and the coefficient of determination of the fit.

is the Stefan-Boltzmann constant. L is the matrix containing the coefficients to build the temperature Laplacian via the dot product. It is built such that its dot product with the temperature returns the sum of the second-order central finite difference in all directions. In the Laplacian matrix, the elements corresponding to the derivative in the diagonal direction are divided by 2, to account for the increase in distance.

Assuming $\alpha(T)$ to be slowly varying, the uncertainty in the temporal variation, diffusion, and radiation terms of the heat equation can be calculated with Eqs. (6)–(8), respectively, for the pixel i,

$$\sigma_{\frac{\partial T}{\partial t}} = \frac{k\, t_f}{\kappa\, dt} \times \sqrt{\left(\frac{\sigma_{C_{i+1}}}{a_1\alpha(T_{i+1})}\right)^2 + \left(\frac{\sigma_{C_{i-1}}}{a_1\alpha(T_{i-1})}\right)^2 + \left[(T_{i+1} - T_{i-1})\frac{\sigma_{a_1}}{a_1}\right]^2}, \tag{6}$$

$$\sigma_{\Delta T} = \frac{k\, t_f}{dx^2}\sqrt{L^2 \cdot \left[\left(\frac{\sigma_{C_i}}{a_1\alpha(T_i)}\right)^2 + \left(\frac{\sigma_{C_0}}{a_1\alpha(T_0)}\right)^2 + \left((T_i - T_0)\frac{\sigma_{a_1}}{a_1}\right)^2\right]}, \tag{7}$$

$$\sigma_{T_i} = \frac{1}{\alpha(T_i)}\sqrt{\frac{(\sigma_{C_i}^2 + \sigma_{C_0}^2)}{a_1^2} + \left[\left(\frac{C_i - C_0}{a_1}\right)\frac{\sigma_{a_1}}{a_1}\right]^2 + (\alpha(T_i)\sigma_{T_0})^2},$$
$$\sigma_{BB} = 4\varepsilon\sigma_{SB}\sqrt{({T_i}^3\sigma_{T_i})^2 + ({T_0}^3\sigma_{T_0})^2}. \tag{8}$$

D. Foil calibration

In this section, the calibration procedure followed to obtain the foil properties will be detailed. To calibrate the foil, its thickness t_f, thermal κ, diffusivity, and black body emissivity ε must

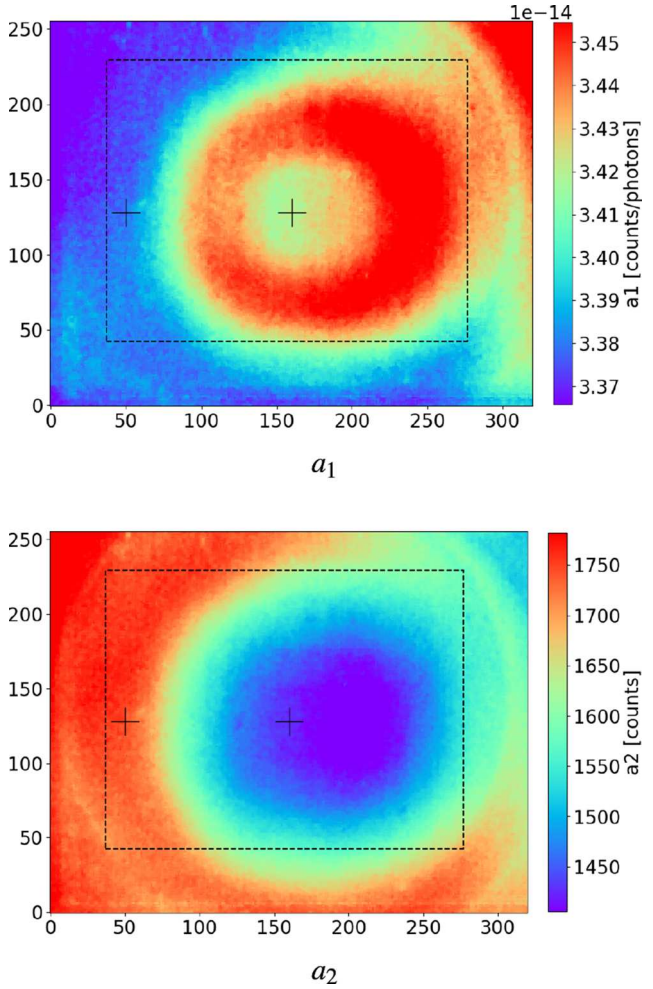

FIG. 14. a_1 and a_2 coefficients of Eq. (3) obtained via calibration with the NUC plate. In black is highlighted the region corresponding approximately to the IRVB foil and the two reference points defined in Fig. 11. The vertical orientation during this calibration is right to left, with the top on the left.

be determined (assuming a nominal platinum thermal conductivity $k = 71.6$ W/mK). A set of spatially resolved parameters was supplied together with the foil, of which the average and variability across the foil correspond to $\varepsilon = 0.85 \pm 0.04, t_f = 1.29 \pm 0.17$ μm. Nominal platinum thermal diffusivity is assumed $\kappa = 2.5 \times 10^{-5}$ m^2/s. These values were obtained with a single exposure of a laser of known power, pulse, and spatial shape by monitoring the cooling down phase of the foil in vacuum, as described in Ref. 28. There are different ways to find the foil parameters, all reliant on shining a laser on the foil (see Refs. 28, 31, and 32).

Rather than using a single laser exposure, the method of choice relied upon varying the laser intensity, frequency, and focus, as done by Reinke.[8] With slow pulses, the time variation component tends to become irrelevant, such that only black body radiation and diffusion remain. With a defocused laser (low laser power density), the temperature increase is low and the spatial distribution

is slowly varying, increasing the relevance of the black body radiation. With a fast pulsed laser, the time-dependent component is dominant.

A bench-top vacuum system was built for the foil calibration, shown in Fig. 15. The vacuum is necessary to eliminate convection as a heat loss mechanism, as it is also absent during the experiments. The pressure during calibration was ~3×10^{-5} bar, compared to ~10^{-8} bar during MAST-U experiments. A 5 mW, 655 nm BlueLyte laser was used, capable of gradually reducing the total power output to zero and with a maximum modulation up to 750 kHz. The laser was equipped with an adjustable lens to change the focus. The laser was calibrated with a Thorlabs PDA100A2 diode in combination with a variable aperture. The maximum laser intensity was measured to be about 1200 and 50 W/m^2 when focused and defocused, respectively, with a maximum total power of 4.16 mW. The laser was controlled with a square wave function generator so that the laser output was modulated in intensity, frequency, and focus. The transmission of the vacuum window on the laser side was measured at 93.3% and taken into account. The power delivered to the foil integrated over the pinhole area, P, can be determined with Eq. (5). To find the foil thermal properties, the running average of P is computed, averaging over the duration of half the square wave duration. The peaks P_h and troughs P_l of the running average are compared to the input values P_{in}.

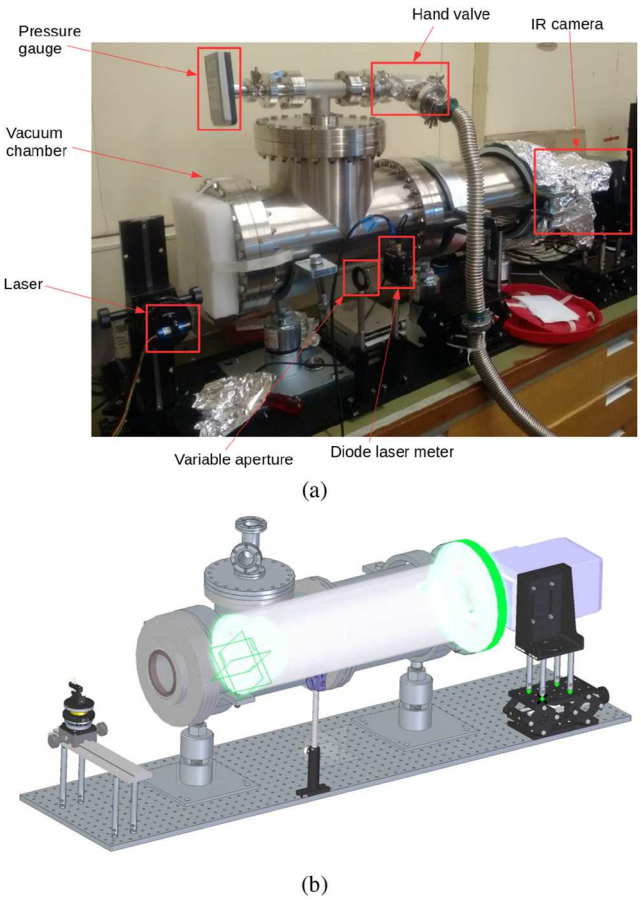

FIG. 15. Photograph (a) and CAD model (b) of the bench-top setup used for the foil calibration. In the CAD model, the re-entrant tube is shown in white, and the foil assembly is on the left side. The photograph, taken on August 02, 2018, shows the laser used to illuminate the foil, as well as the diode and aperture used to calibrate the laser and vacuum system.

A scan in laser power from 0% to 100% and frequency from 0.2 to 90 Hz with the laser fully focused and fully defocused was carried out in the location of the foil closer to the pinhole. The fit was done with data up to 10 Hz, returning the following fit parameters: $\varepsilon = 1, t_f = 2.69\ \mu$m, $\kappa = 1.35 \times 10^{-5}$ m^2/s. The t_f/κ ratio is similar to foil properties measured prior to the installation on NSTX-U, differing significantly from the supplied one.[25] The difference in the t_f and κ values is likely due to the difference in emissivity inferred.

An example of the power calculated in the laser experiments is shown in Fig. 16, while Fig. 17 shows the quality of the fit for varying power and frequency and for focused and defocused laser light. It can be observed that above 30 Hz, the inferred power drops, implying a limit in the temporal resolution of the IRVB. The data corresponding to the defocused laser degrades at lower frequencies as the total delivered laser power is lower. During these experiments, it was also observed that a fixed oscillation of 0.01 K at about 29 Hz is superimposed on the data, so measurements at the same frequency or higher will be affected. The oscillation seems to be independent of the power supply system and the frame rate but proportional to the integration time, ultimately due to the internal operation of the camera.

These foil properties were measured in a single location and were therefore assumed to be uniform across the foil. To account for the variability across the foil, the uncertainty from the fit is increased by the variability of the properties provided to us with the foil. This returns the uncertainties $\sigma_\varepsilon/\varepsilon = 8.61\%, \sigma_{t_f}/t_f = 13.6\%$, $\sigma_\kappa/\kappa = 13.9\%$ (for κ is used the same variability across the foil as for t_f).

E. Viewing geometry validation

The viewing geometry of the diagnostic as designed in Sec. III has to be validated to make sure that each IRVB pixel FOV into the plasma is as expected. For diagnostics, where a camera is directly imaging inside the vacuum vessel, this is usually done by acquiring long exposure images and matching the observed features on the machine surface with features from computer-aided design (CAD) models. For bolometers, this is not possible, as the black body radiation of the vessel surfaces is many orders of magnitude below the detection limit, even when heated up by the plasma. For this reason, this spatial calibration has to rely on laser light sources. The size and orientation of the LOS viewing cone are often measured in dedicated laboratory experiments and translated into machine coordinates using some reference points from the diagnostic assembly and the vessel.[33,34] If there is good access to the inside of the machine, a laser can be placed in fixed locations to measure the bounds of the light detection region of every LOS.[35] More recently, in the effort to develop the bolometer system for ITER, a robotic arm was developed on AUG, which can probe the relation between the origin of the emission and sensor response by moving a laser to various positions in the field of view of the bolometer.[36] An inability to access

the interior of MAST-U prevented these types of measurements. For these reasons, the geometry of the IRVB was verified by comparing known features of the plasma during operation with their expected locations, adapting methods used for visible imaging. The bright features of interest are the fueling locations, the alignment of the center column, and the flash heating of the foil during disruptions.

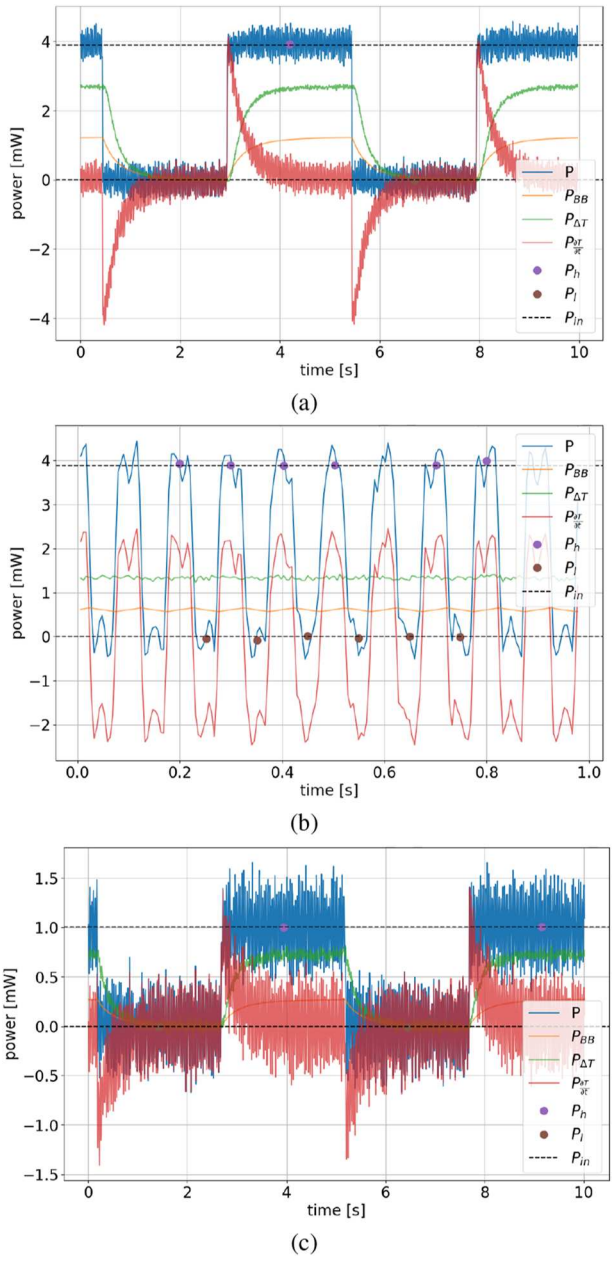

FIG. 16. Examples of the power absorbed by the foil and its components (total absorbed power P and its components black body radiation P_{BB}, conduction $P_{\Delta T}$ and temperature variation $P_{\frac{\partial T}{\partial t}}$; peaks and troughs of P running average, P_h and P_l; peak input power P_{in}) with the laser at maximum intensity for a focused low frequency case (a), a focused high frequency case (b), and a defocused low frequency one (c).

1. Spatial calibration using fueling valves and EFIT++

The plasma can be fueled via a multitude of entry ports, of which only some are directly visible by the IRVB. The names of the valves corresponding to the visible outlets are indicated in Fig. 7. If hot plasma is present in the immediate vicinity of the gas outlet, the hot electrons dissociate and then excite and ionize the injected neutrals. If the electron temperature is not too high and the plasma is close enough, a bright non-toroidally symmetric emission appears in the vicinity of the gas outlet. In all the observed discharges when the gas injection valve PFR_BOT_B01 was employed, a localized bright region never appeared, possibly because the separatrix was too far away or the gas flow was too low. The fueling valves, then, that caused a visible localized emission to appear in the IRVB FOV are HFS_MID_L08 and HFS_BOT_B03, although HFS_BOT_B03 was only used once and thus not very useful to compare across pulses.

The two HFS_MID_L08 valve outlet locations at the inner wall can be used as one spatial calibration of the IRVB viewing geometry. The valve is consistently used throughout MU01, and its outlets are both in the field of view of the high-speed visible light camera (HSV), shown in Fig. 18, while only one outlet is in the IRVB FOV.

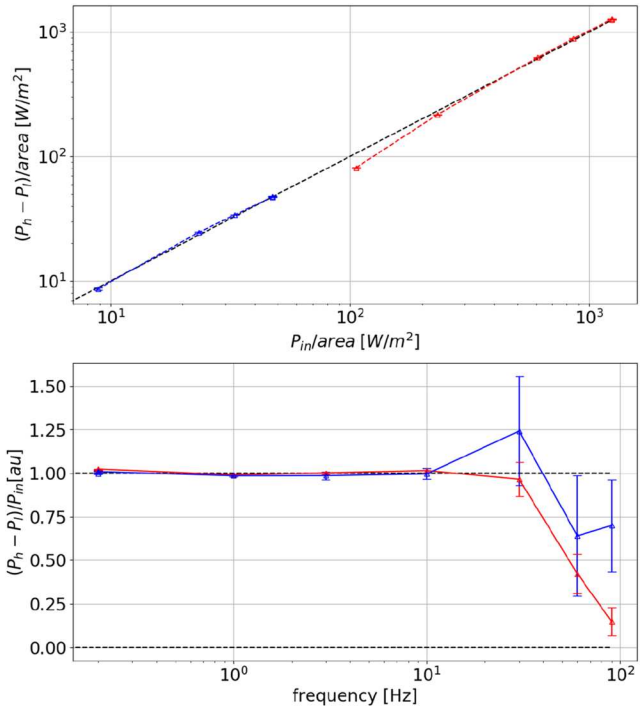

FIG. 17. Variation of the measured power compared to the expected values with laser intensity (top) and frequency (bottom). The blue color indicates the defocused cases, while the red indicates the focused ones. P_h and P_l are the inferred high and low power levels of the laser square wave, *area* is the area of the foil receiving laser light, and P_{in} is the known peak laser power density.

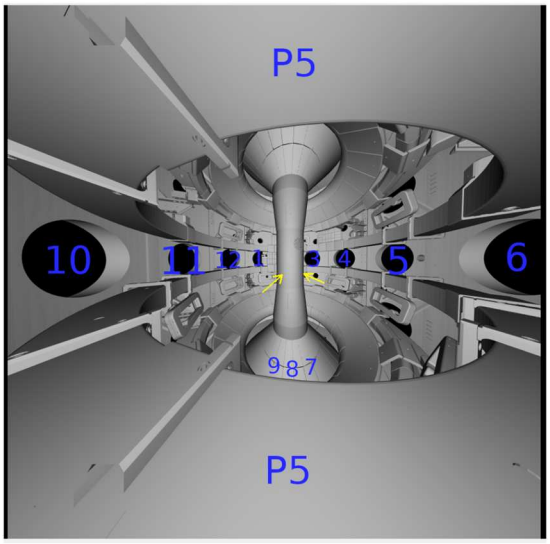

FIG. 18. Field of view of the high-speed visible light camera, indicating the sector numbers. In yellow, the locations of the outlets of the gas valve HFS_MID_L08 are indicated.

Strong visible light brightness does not necessarily indicate a strong total radiated power, but indicates regions where neutral hydrogen is interacting with the plasma.[37]

Figure 19 shows the comparison of the localized emission arising from the use of valve HFS_MID_L08 for HSV and IRVB for the shot 45351. Figure 19(a) shows the brightness from the IRVB while Fig. 19(b) shows the brightness from the HSV. The IRVB shows that the emissivity is clearly non-symmetric and localized in the proximity of the outlet. The HSV data are affected by saturation, but the bright spot due to both outlets is clearly visible. To further illustrate the validity of the comparison, Fig. 19(b) shows the time evolution of the average of the relative brightness around outlets compared to the flow rate of gas programmed for the valve. Both IRVB and HSV measure an increase and decrease in the local emissivity that matches the gas output.

Figure 20 shows a later stage of the discharge when the HFS_MID_L08 valve is off. The image, determined with EFIT++ magnetic reconstruction,[38] shows that high emissivity regions are present along the inner and outer legs, as would be expected in the divertor for a detached target. This consistency is true across all shots, providing further indication of the similarity of the real IRVB geometry to the designed one.

2. Spatial calibration using disruptions

During disruptions, the core plasma can quickly move toward plasma-facing components (PFC). There, the ion flux is recycled as neutrals, which are then excited through electron–atom interactions, leading to a strong localized radiation from the proximity of the PFCs in question. Additionally, some carbon can be sputtered from the PFCs because of the sudden increase in particle flux, which can also lead to radiation from the excited C ions and neutrals. Because

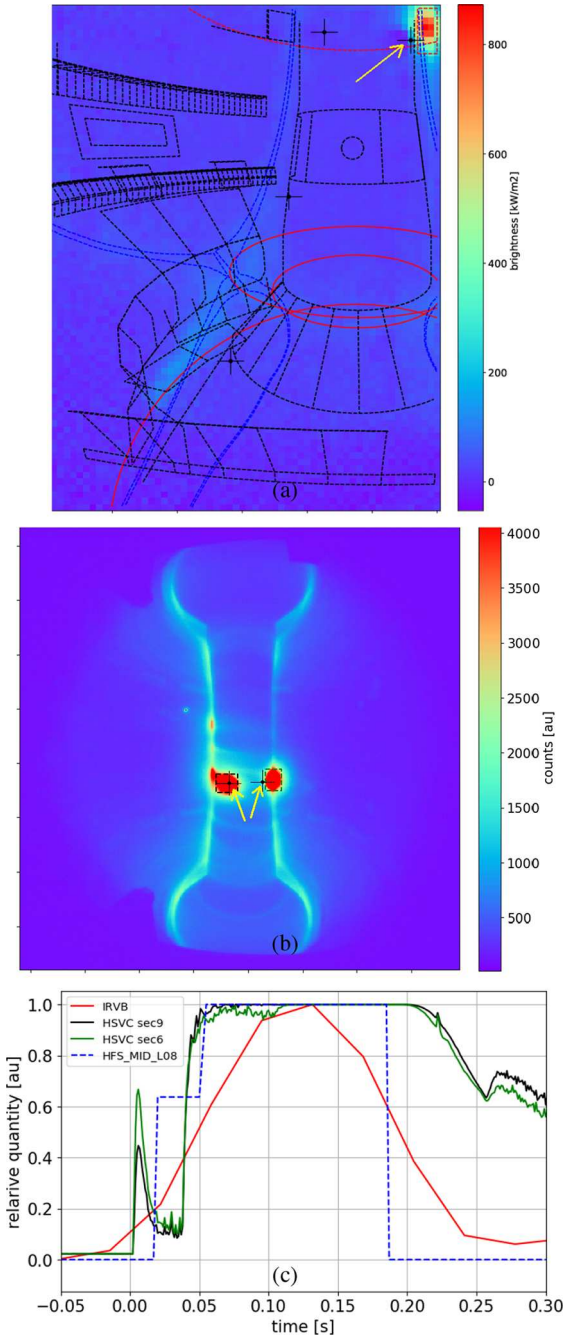

FIG. 19. Example of the radiation caused by the valve HFS_MID_L08 from shot 45295. (a) brightness data from IRVB at 132 ms. Shown in dashed blue is the poloidal projection of the separatrix. The toroidal traces of the x-point and strike points are shown in solid red, and in dashed red is the magnetic axis. The outlet of the valve HFS_MID_L08 in the IRVB FOV, marked by a black cross and a yellow arrow, is clearly visible in the IRVB image. In (b), a cropped image of the raw data from the high-speed visible light camera (HSV) for the same shot at 50 ms. The two bright spots correspond to the two outlets from the valve, both in the HSV FOV, marked as in (c). Note: these data are affected by saturation. In (d), the relative average of the readings inside the dashed regions that are outlined in (a) and (b), and the programmed flow for the HFS_MID_L08 valve.

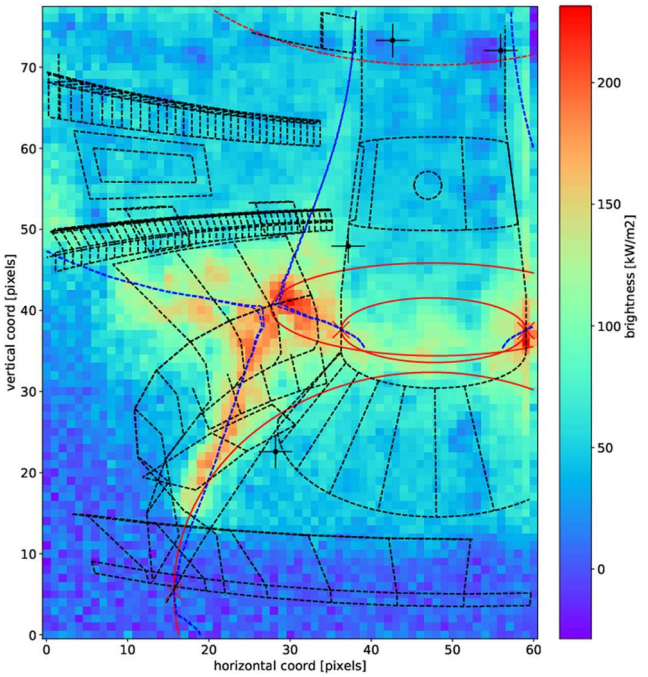

FIG. 20. IRVB Brightness image of the plasma from shot 45295, 388 ms, at a time when high field side valves are off and the target is radiatively detached. In blue, a tangential projection shows the separatrix from EFIT++ magnetic reconstruction overlaid on the image using nominal IRVB design geometry. The toroidal traces of the x-point and strike points are shown in solid red, and in dashed red is the magnetic axis.

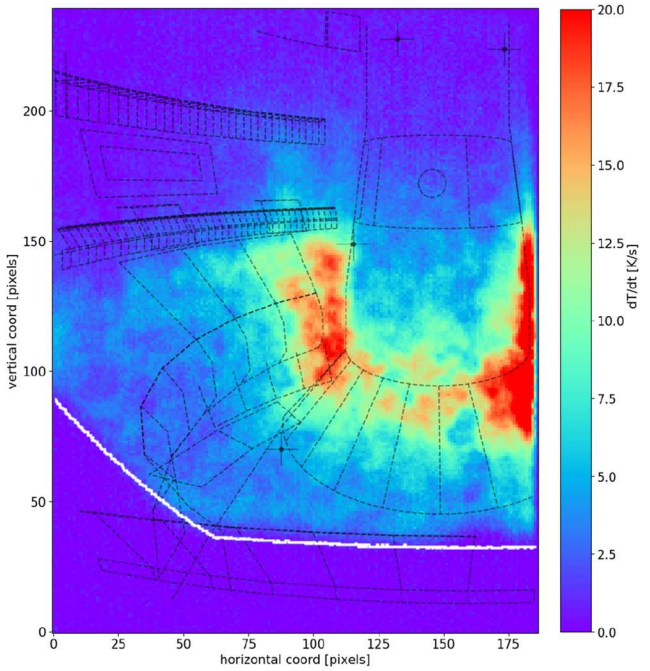

FIG. 21. Image of the foil temperature increasing due to the disruption of the plasma in shot 45225. No temporal or spatial binning of the data applied. Indicated in white is the demarcation line between the region of the foil that receives any radiation or none from a homogeneous emitter in the core and divertor regions of Fig. 5.

of the transient nature of the phenomenon, it is sufficient to investigate the temporal derivative of the foil temperature, neglecting the other components of the heat transfer equation, to locate regions where a high emission originates.

Figure 21 shows the foil temperature increase due to a disruption at the end of shot 45225. The plasma moved toward the lower half of the machine, and as a consequence, a strong emission comes from regions of the image within close proximity to the tiles. Details of the radiation structure can't be easily interpreted as the source of the signal is not necessarily toroidally symmetric. A bright emission is present close to the tiles around the baffle, and it is therefore possible to observe the presence of a part of the foil that cannot be illuminated because of the interference of the P6 coil close to the pinhole seen in Fig. 7. The demarcation line between the region of the foil that can or cannot receive radiation in Fig. 5 is overlaid, and it lines up well with the observation.

From the above observations, it can be stated that the IRVB is positioned "close" to what is expected from the design; we cannot be quantitative in determining how accurate the view of each pixel is. The FOV calibration could be further improved by including the valve HFS_MID_L02 and modifying the geometry such that the observation in Fig. 5 has an even better match with Fig. 21, but a confirmation of the geometry as per design is for now sufficient.

V. RESULTS

Once the IR camera, the foil, and the viewing geometry are validated, the IRVB can be used to measure the radiation brightness (and emissivity) from the plasma during experiments. The data are first split between the two digitizers, and the counts are converted to temperature as per Sec. IV A. As mentioned in Sec. IV D, the camera is affected by a pickup oscillation of the signal at a frequency of about 29 Hz, so the temperature is binned in time over one period of such oscillation, returning a temporal resolution of about 30 ms. In order to reduce the noise, the temperature is also binned spatially over the foil, with a good compromise between resolution and noise being a 3×3 pixel binning, reducing the independent LOS in the plasma from 36 700 to about 3900. The binned temperature is then used to calculate the power absorbed by the foil, and the result from the two digitizers is averaged. Finally, the power is converted to brightness by multiplying by 4π/etendue.

In conventionally diverted discharges[39] in which the core density was progressively increased with either fueling from the midplane or the divertor, it can be observed that the peak brightness is at first close to the targets before moving along the divertor legs to the x-point, forming what has been called an x-point radiator configuration (XPR)[40] or an X-point MARFE (for multifaceted asymmetric radiation from the edge).[41,42] On further increase in the density, the radiation moves upstream along the inner separatrix to a region around the midplane, where a toroidally symmetric MARFE-like structure forms at the high field side (HFS) of the plasma.[42] From

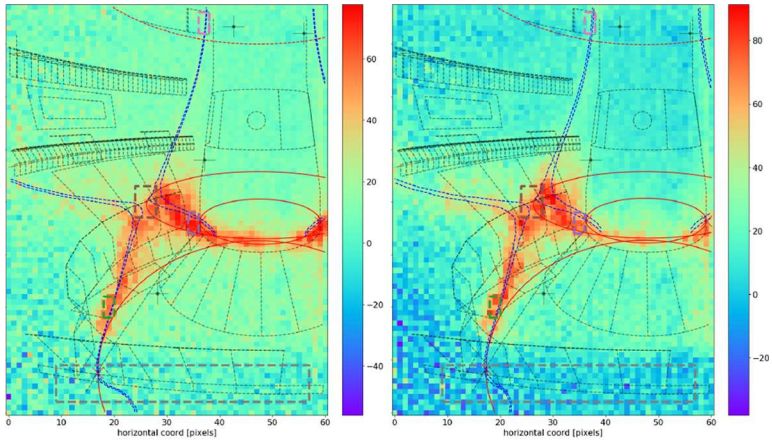

(a) 386ms (b) 511ms

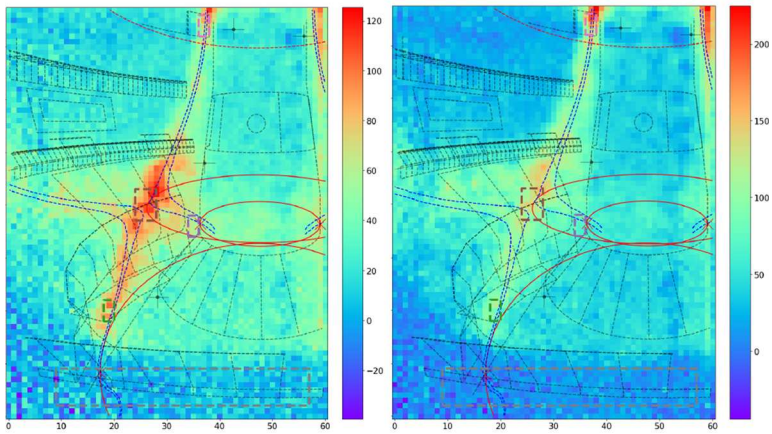

(c) 605ms (d) 699ms

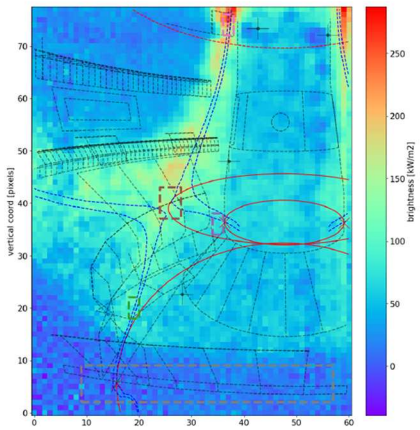

(e) 762ms

FIG. 22. Changes in brightness pattern in a density ramp for a conventional divertor, L-mode, and Ohmic plasma (shot 45473, Double-null, and 600 kA). First, the inner target is radiatively attached (a), then it starts detaching (b) to form an x-point radiator (c), and finally a radiation MARFE-like structure on the high field side (HFS) midplane (d). Further increasing the density, the structure moves inward (e), leading to a disruption. Note that all the images have different color bar ranges. The average brightness in the regions marked by the dashed lines (green: outer target, violet: inner target, brown: x-point, pink: midplane, gray: control) will be used for later analysis.

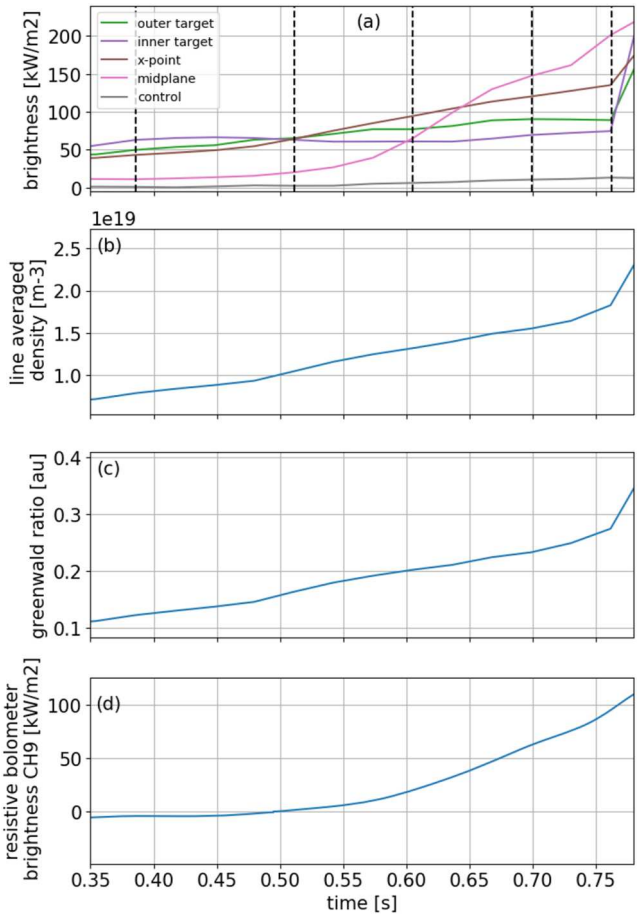

FIG. 23. Comparison of the measurements from different diagnostics for the shot 45473. In (a), the IRVB brightness is averaged inside the regions indicated with dashed lines of matching colors around the x-point and other regions in Fig. 22 while the vertical black lines indicate the time corresponding to the images in Fig. 22. In (b), the core line averaged density, (c) is the Greenwald density ratio, and (d) is the brightness from the resistive bolometer core toroidal channel 9.

there, the structure becomes brighter and moves slowly inward from the inner wall, correlating with the ensuing disruption.

These phases are shown for the double-null low-power Ohmic shot 45473 in Fig. 22. The movement of the radiation can be correlated with other plasma parameters like the core plasma density and with the existing resistive bolometry system, for which the chordal views are shown in Fig. 8. For MU01, multiple LOSs of the resistive bolometers were damaged, and the measurements were severely affected by noise, but the system was robust enough to return low-time resolution data. The two LOS closest to the x-point are not available, but the one just below the midplane (CH9, see Fig. 8) is.

Figure 23 shows the comparison between resistive bolometry CH9 chordal brightness and similar brightness measurements from the IRVB. Figure 23(a) shows the average IRVB brightness inside the regions marked with matching colors in Fig. 22 vs time. The region with the highest brightness changes with time according to the time development described for Fig. 22. This is related to the monotonic increase in the core density that causes the plasma to detach from the targets. The brightness from the resistive bolometer CH9 [Fig. 23(d)] has to be compared with the midplane data from the IRVB [Fig. 23(a)]. The absolute value of the brightness is different, with the IRVB recording about two times the brightness of the resistive bolometer (possibly because the LOS of the IRVB is integrated over a much longer path through the plasma). Most importantly, though, the emission starts to rise for both at ~550 ms and at a similar rate, indicating that both are observing the same phenomena. An important observation to demonstrate the absence of systematic errors is to check the region of the foil that should not receive radiation from the plasma shown in Fig. 5. This is labeled *control* in Fig. 23, and while drifting upward in time, it is much smaller than the relevant quantities. This region can also be used to measure the noise level of the diagnostic. The measured NEPD, with the binning mentioned above, is 0.79 W/m^2, close to that indicated by previous models (0.58 W/m^2 from Ref. 43) and below initial expectations. The uncertainty on the power density with the same binning, whose estimate includes the uncertainty on the foil parameters and the camera calibration, has a minimum of about 10 W/m^2, gradually increasing with a stronger signal up to about 30 W/m^2 in Fig. 24(d).

In higher-power discharges, like when the NBI is used and H-mode can be achieved, a similar sequence of events happens to that shown and discussed above for L-mode plasmas and detachment. This is demonstrated in Fig. 24, which shows the change in IRVB brightness pattern for a conventional divertor-beam heated discharge. The sequence proceeds as for the lower-power one, except that after the HFS MARFE-like structure is developed, the core density decreases and the peak radiation moves back closer to the x-point. The brightness is much higher than in Fig. 22 because of the increase in heating power. In Fig. 24(a), a region at the top left of the image that shows strong brightness but does not seem field aligned can be observed. This region typically has strong brightness in beam-heated discharges before and after the H-mode phase. Similar behavior was also observed in resistive bolometry for LOS aimed in the direction opposite to the NBI. The origin of this effect is unclear, but it is possible that the heat flux is associated with fast particles escaping the core plasma and undergoing charge exchange. This could be verified by comparing the brightness of the region of interest with data from the fast ion loss detector diagnostic or results from modeling, but it is outside the scope of this manuscript.

Figure 25 shows the relevant time traces for shot 45401. The density is much higher, and the Greenwald fraction (a metric of the tokamak performance such that the maximum usually achievable is 1[44]) corresponding to radiative detachment is around 0.6 rather than 0.15 as for the lower power shot 45473. Here, the comparison with resistive bolometry can be done both at the midplane (CH9) as well as close to the location on the separatrix labeled intermediate that corresponds to channels 13 and 14 (CH13, CH14). Agreement is good at the midplane but not as good in the intermediate position, where CH13 and CH14 detect significant radiation even before ~850 ms, unlike IRVB. The difference is likely not due to the NBI, as only the leftmost part of the foil is affected, and also only the outermost counter-NBI resistive bolometer LOS is affected [see Fig. 8(b)], while it could be due to a different length of the resistive bolometer

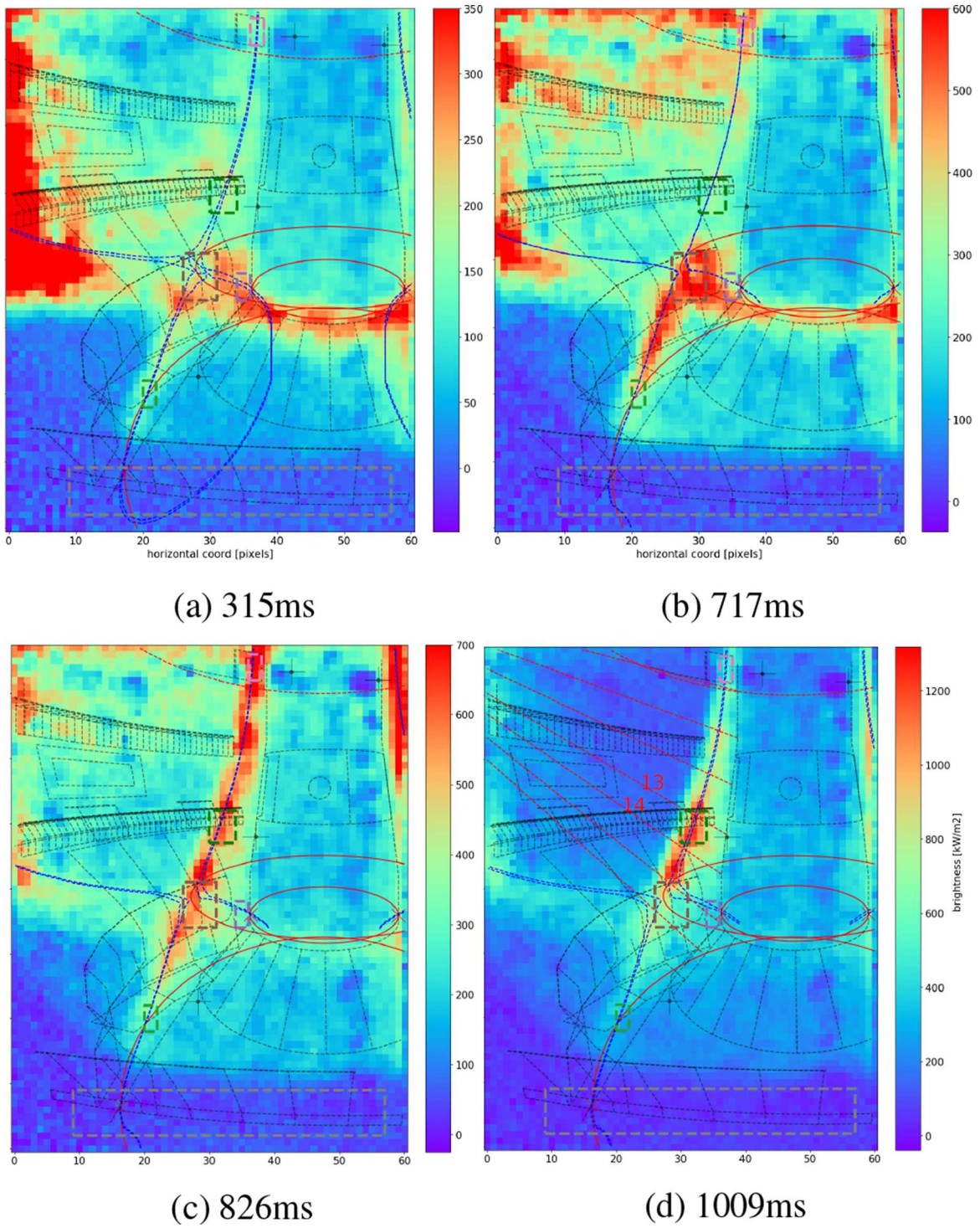

FIG. 24. Changes in brightness pattern in a density ramp for a conventional divertor, H-mode, beam-heated plasma (shot 45401, Double-null, and 750 kA). First, the inner target is radiatively attached (a). Then, it detaches and forms an x-point radiator (b) and finally a radiation MARFE-like structure on the HFS midplane (c). In this shot, the density was decreased after this point and this resulted in the peak radiation to move back toward the x-point (d). The bright region at the top left of (a) is likely due to the foil being heated by a particle flux rather than radiation from the plasma. In (d) are overlaid in dashed red and numbered, the resistive bolometer LOS through similar regions as included in the IRVB brightness image shown. Note that all images have different color bar ranges. The average brightness in the regions marked by the dashed lines (green: outer target, violet: inner target, brown: x-point, pink: midplane, gray: control) will be used for later analysis.

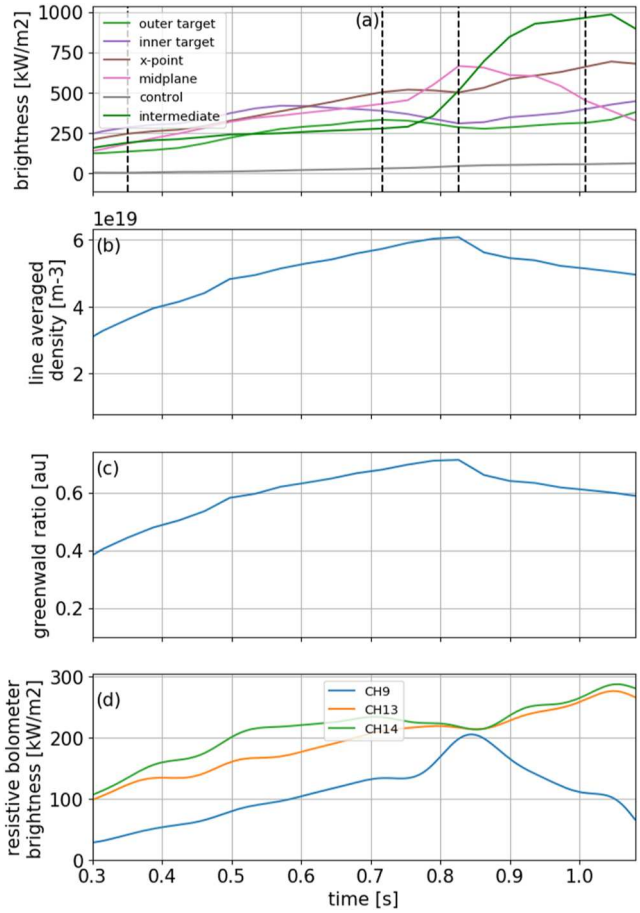

FIG. 25. Comparison of the measurements from different diagnostics for the shot 45401. In (a), the IRVB brightness is averaged inside the regions indicated with dashed lines in Fig. 24, while the black lines indicate the time corresponding to the images in Fig. 24. In (b), the core line is averaged density, (c) is the Greenwald density ratio, and (d) is the brightness from the resistive bolometer core toroidal channels 9, 13, and 14, where the first corresponds to the midplane, while the others to the intermediate regions of the IRVB.

LOS in the emitting region or because it is detecting some radiation from the inner leg (CH14 could be more affected than CH13, hence the higher brightness in CH14).

VI. SUMMARY

The IRVB diagnostic was successfully deployed in MAST-U. This represents a new implementation of the bolometric diagnostic, not only because it is the first use on a spherical tokamak device but also because it is aimed at measuring the total radiation emissivity in the region of the x-point, where significant spatial gradients are expected and a high spatial resolution is necessary. The choices that guided the design of all aspects of the diagnostic are reported, with lessons learned for future implementations. The calibration procedures are detailed, including the verification that the IRVB positioning, viewing geometry, and FOV qualitatively match the design after installation, normally a challenging task for bolometers. The early results from the first MAST-U experimental campaign show that the evolution of detachment in a spherical tokamak follows similar trends as for low aspect ratio ones, at least for the conventional divertor. In the first MAST-U campaign (MU01) discharges, with only intrinsic impurities, the radiation peaks move along the two divertor legs and the HFS separatrix depending on the level of detachment. The x-point radiator was observed as an intermediate stage before the peak of the radiation moved upstream along the inner separatrix up to the HFS midplane, forming a toroidally symmetric MARFE-like structure. It was also verified that the IRVB measurements are roughly consistent with resistive bolometry. To further exploit the diagnostic, it will be necessary to perform tomographic inversions of the line-integrated data to observe the evolution of the poloidal emissivity profile with changes in the core plasma density. This will allow the inner and outer legs to be examined in more detail and demonstrate the expected high spatial resolution from the IRVB. Simplified integral methods exist to extract an approximate total radiated power without the need for a full tomographic inversion[45] but are out of scope here. Tomographically inverted data and inferences from it will be presented in a future publication dedicated to the scientific exploitation of the diagnostic.

ACKNOWLEDGMENTS

This work was supported by U.S. Department of Energy Award Nos. DE-AC05-00OR22725 and DESC0014264 and under the auspices of the Engineering and Physical Sciences Research Council (Grant Nos. EP/L01663X/1 and EP/W006839/1). To obtain further information on the data and models underlying this paper, please contact PublicationsManager@ukaea.uk.

Support for M. L. Reinke's contributions was in part provided by Commonwealth Fusion Systems.

This work has been carried out within the framework of the EUROfusion Consortium, funded by the European Union via the Euratom Research and Training Program (Grant Agreement No. 101052200-EUROfusion). The views and opinions expressed are, however, those of the author(s) alone and do not necessarily reflect those of the European Union or the European Commission. Neither the European Union nor the European Commission can be held responsible for them.

The authors wish to also acknowledge Byron J. Peterson for providing the blackened and calibrated platinum foil used as an absorber in the IRVB.

AUTHOR DECLARATIONS

Conflict of Interest

The authors have no conflicts to disclose.

Author Contributions

Fabio Federici: Conceptualization (supporting); Data curation (lead); Formal analysis (lead); Funding acquisition (supporting); Investigation (lead); Methodology (equal); Project administration (equal); Resources (supporting); Software (lead); Validation (lead); Visualization (lead); Writing – review & editing (lead). **Matthew**

L. Reinke: Conceptualization (lead); Formal analysis (supporting); Funding acquisition (lead); Investigation (supporting); Methodology (equal); Project administration (equal); Resources (supporting); Supervision (lead); Validation (supporting); Writing – original draft (lead); Writing – review & editing (supporting). **Bruce Lipschultz**: Formal analysis (supporting); Funding acquisition (equal); Investigation (equal); Resources (equal); Supervision (lead); Writing – original draft (supporting). **Andrew J. Thornton**: Conceptualization (equal); Funding acquisition (lead); Project administration (equal); Writing – review & editing (lead). **James R. Harrison**: Data curation (supporting); Formal analysis (supporting); Software (supporting). **Jack Lovell**: Funding acquisition (supporting); Investigation (equal); Project administration (supporting); Resources (supporting); Validation (equal). **Matthias Bernert**: Funding acquisition (supporting); Project administration (supporting).

DATA AVAILABILITY

Raw data were generated at the MAST Upgrade large scale facility. Derived data supporting the findings of this study are available from the corresponding author upon reasonable request.

REFERENCES

[1] M. Faitsch, T. Eich, G. F. Harrer, E. Wolfrum, D. Brida, P. David, M. Griener, and U. Stroth, "Broadening of the power fall-off length in a high density, high confinement H-mode regime in ASDEX Upgrade," Nucl. Mater. Energy **26**, 100890 (2021).

[2] D. Silvagni, T. Eich, M. Faitsch, T. Happel, B. Sieglin, P. David, D. Nille, L. Gil, and U. Stroth, "Scrape-off layer (SOL) power width scaling and correlation between SOL and pedestal gradients across L, I and H-mode plasmas at ASDEX Upgrade," Plasma Phys. Controlled Fusion **62**(4), 045015 (2020).

[3] A. Q. Kuang, S. Ballinger, D. Brunner, J. Canik, A. J. Creely, T. Gray, M. Greenwald, J. W. Hughes, J. Irby, B. LaBombard, B. Lipschultz, J. D. Lore, M. L. Reinke, J. L. Terry, M. V. Umansky, D. G. Whyte, and S. Wukitch, "Divertor heat flux challenge and mitigation in SPARC," J. Plasma Phys. **86**, 865860505 (2020).

[4] A. Loarte, B. Lipschultz, A. S. Kukushkin, G. F. Matthews, P. C. Stangeby, N. Asakura, G. F. Counsell, G. Federici, A. Kallenbach, K. Krieger, A. Mahdavi, V. Philipps, D. Reiter, J. Roth, J. Strachan, D. G. Whyte, R. Doerner, T. Eich, W. Fundamenski, A. Herrmann, M. Fenstermacher, P. Ghendrih, M. Groth, A. Kirschner, S. Konoshima, B. LaBombard, P. Lang, A. W. Leonard, P. Monier-Garbet, R. Neu, H. Pacher, B. Pegourie, R. A. Pitts, S. Takamura, J. L. Terry, and E. Tsitrone, "Chapter 4: Power and particle control," Nucl. Fusion **47**(6), S203 (2007).

[5] A. S. Kukushkin, H. D. Pacher, G. W. Pacher, V. Kotov, R. A. Pitts, and D. Reiter, "Consequences of a reduction of the upstream power SOL width in ITER," J. Nucl. Mater. **438**(SUPPL), S203–S207 (2013).

[6] B. Lipschultz, J. L. Terry, C. Boswell, J. A. Goetz, A. E. Hubbard, S. I. Krasheninnikov, B. LaBombard, D. A. Pappas, C. S. Pitcher, F. Wising, and S. Wukitch, "The role of particle sinks and sources in Alcator C-Mod detached divertor discharges," Phys. Plasmas **6**(5), 1907–1916 (1999).

[7] F. Reimold, M. Wischmeier, M. Bernert, S. Potzel, A. Kallenbach, H. W. Müller, B. Sieglin, and U. Stroth, "Divertor studies in nitrogen induced completely detached H-modes in full tungsten ASDEX Upgrade," Nucl. Fusion **55**(3), 033004 (2015).

[8] M. L. Reinke, J. L. Terry, G. G. van Eden, B. J. Peterson, K. Mukai, T. K. Gray, and B. C. Stratton, "Experimental tests of an infrared video bolometer on Alcator C-Mod," Rev. Sci. Instrum. **89**(10), 103507 (2018).

[9] J. M. Gao, Y. Liu, W. Li, J. Lu, Y. B. Dong, Z. W. Xia, P. Yi, and Q. W. Yang, "Minimum Fisher regularization of image reconstruction for infrared imaging bolometer on HL-2A," Rev. Sci. Instrum. **84**(9), 093503 (2013).

[10] B. J. Peterson, S. Konoshima, H. Parchamy, M. Kaneko, T. Omori, D. C. Seo, N. Ashikawa, and A. Sukegawa, "Observation of divertor and core radiation in JT-60U by means of bolometric imaging," J. Nucl. Mater. **363-365**(1-3), 412–415 (2007).

[11] J. Jang, W. Choe, B. J. Peterson, D. C. Seo, K. Mukai, R. Sano, S. Oh, S. H. Hong, J. Hong, and H. Y. Lee, "Tomographic reconstruction of two-dimensional radiated power distribution during impurity injection in KSTAR plasmas using an infrared imaging video bolometer," Curr. Appl. Phys. **18**(4), 461–468 (2018).

[12] B. J. Peterson, S. Oh, D. Seo, J. Jang, J. S. Park, K. Mukai, and W. Choe, "Signal to noise ratio of upgraded imaging bolometer for KSTAR," Rev. Sci. Instrum. **89**(10), 10E115 (2018).

[13] B. J. Peterson, "Infrared imaging video bolometer," Rev. Sci. Instrum. **71**(10), 3696–3701 (2000).

[14] B. J. Peterson, E. A. Drapiko, D. Seo, and N. Ashikawa, "Upgrade of imaging bolometers on LHD," Plasma Fusion Res. **5**, S2095.1–S2095.4 (2010).

[15] A. Miyashita, K. Mukai, S. Ohshima, R. Matoike, B. J. Peterson, S. Kobayashi, H. Okada, S. Kado, T. Minami, T. Mizuuchi, S. Konoshima, and K. Nagasaki, "First application of an InfraRed imaging video bolometer to Heliotron J plasma," Plasma Fusion Res. **16**, 1202079-1 (2021).

[16] K. F. Mast, J. C. Vallet, C. Andelfinger, P. Betzler, H. Kraus, and G. Schramm, "A low noise highly integrated bolometer array for absolute measurement of VUV and soft x radiation," Rev. Sci. Instrum. **62**(3), 744–750 (1991).

[17] S. N. Pandya, B. J. Peterson, R. Sano, K. Mukai, E. A. Drapiko, A. G. Alekseyev, T. Akiyama, M. Itomi, and T. Watanabe, "Calibration of a thin metal foil for infrared imaging video bolometer to estimate the spatial variation of thermal diffusivity using a photo-thermal technique," Rev. Sci. Instrum. **85**(5), 054902 (2014).

[18] K. Mukai, B. J. Peterson, N. Ezumi, N. Shigematsu, S. Ohshima, A. Miyashita, and R. Matoike, "Sensitivity improvement of infrared imaging video bolometer for divertor plasma measurement," Rev. Sci. Instrum. **92**(6), 063521 (2021).

[19] B. L. Henke, E. M. Gullikson, and J. C. Davis, "X-ray interactions: Photoabsorption, scattering, transmission, and reflection at $E = 50–30\,000$ eV, $Z = 1–92$," At. Data Nucl. Data Tables **54**(2), 181–342 (1993).

[20] K. Mukai, B. J. Peterson, S. Takayama, and R. Sano, "*In situ* calibration of the foil detector for an infrared imaging video bolometer using a carbon evaporation technique," Rev. Sci. Instrum. **87**, 11E124 (2016).

[21] G. G. van Eden, M. L. Reinke, B. J. Peterson, T. K. Gray, L. F. Delgado-Aparicio, M. A. Jaworski, J. Lore, K. Mukai, R. Sano, S. N. Pandya, and T. W. Morgan, "Design and characterization of a prototype divertor viewing infrared video bolometer for NSTX-U," Rev. Sci. Instrum. **87**(11), 11D402 (2016).

[22] C. Giroud, A. Meakins, M. Carr, A. Baciero, and C. Bertrand (2018)."CHERAB spectroscopy modelling framework," Zenodo. http://doi.org/10.5281/zenodo.1206142

[23] M. Carr, A. Meakins, A. Baciero, M. Bernert, A. Callarelli, A. Field, C. Giroud, J. Harrison, N. Hawkes, S. Henderson, B. Lipschultz, T. Lunt, D. Moulton, and F. Reimold, "Towards integrated data analysis of divertor diagnostics with ray-tracing," in *44th EPS Conference on Plasma Physics, June 2017* (European Physical Society, 2017), p. 2017.

[24] A. Meakins and M. Carr (2017). "Raysect Python raytracing package," Zenodo. http://doi.org/10.5281/zenodo.1205064

[25] M. L. Reinke, "Experimental tests of an infrared video bolometer on Alcator C-mod," in *22nd Topical Conference on High Temperature Plasma Diagnostics* (Oak Ridge National Laboratory, San Diego, USA, 2018).

[26] F. Federici, J. Harrison, T. Farley, and A. J. Thornton (2022). "Analysis routines for the paper 'Design and implementation of a prototype infrared video bolometer (IRVB) in MAST Upgrade,'" Zenodo. Culham, UK. https://zenodo.org/record/7108499

[27] J. F. Rivero-Rodriguez, M. Garcia-Munoz, L. Sanchis, R. Martin, K. G. McClements, R. J. Akers, A. Snicker, J. Ayllon-Guerola, J. Buchanan, P. Cano-Megias, J. Galdon-Quiroga, D. Garcia-Vallejo, and J. Gonzalez-Martin, "Development and installation of a scintillator based detector for fast-ion losses in the MAST-U tokamak," in *45th EPS Conference on Plasma Physics, EPS, July 2018* (European Physical Society, 2018), pp. 233–236.

[28] M. Itomi, B. J. Peterson, Y. Yamauchi, R. Sano, K. Mukai, and S. N. Pandya, "Improvement on infrared imaging video bolometer by laser calibration method," Plasma Fusion Res. **9**(SpecialIssue2), 3406080 (2014).

[29]G. G. Van Eden, M. L. Reinke, S. Brons, G. van der Bijl, B. Krijger, R. Lavrijsen, S. P. Huber, R. Perillo, M. C. M. van de Sanden, and T. W. Morgan, "Plasma radiation studies in Magnum-PSI using resistive bolometry," Nucl. Fusion **58**(10), 106006 (2018).
[30]E. Havlíčková, J. Harrison, B. Lipschultz, G. Fishpool, A. Kirk, A. J. Thornton, M. Wischmeier, S. Elmore, and S. Allan, "SOLPS analysis of the MAST-U divertor with the effect of heating power and pumping on the access to detachment in the Super-x configuration," Plasma Phys. Controlled Fusion **57**(11), 115001 (2015).
[31]R. Sano, B. J. Peterson, E. A. Drapiko, D. Seo, Y. Yamauchi, and T. Hino, "Foil calibration for IR imaging bolometer by laser irradiation," Plasma Fusion Res. **7**(SPL.ISS.1), 2405039 (2012).
[32]F. Cernuschi, A. Russo, L. Lorenzoni, and A. Figari, "In-plane thermal diffusivity evaluation by infrared thermography," Rev. Sci. Instrum. **72**(10), 3988–3995 (2001).
[33]K. McCormick, A. Huber, L. C. Ingesson, F. Mast, J. Fink, W. Zeidner, A. Guigon, and S. Sanders, "New bolometry cameras for the JET enhanced performance phase," Fusion Eng. Des. **74**(1-4), 679–683 (2005).
[34]A. Huber, K. McCormick, P. Andrew, P. Beaumont, S. Dalley, J. Fink, J. C. Fuchs, K. Fullard, W. Fundamenski, L. C. Ingesson, F. Mast, S. Jachmich, G. F. Matthews, P. Mertens, V. Philipps, R. A. Pitts, S. Sanders, and W. Zeidner, "Upgraded bolometer system on JET for improved radiation measurements," Fusion Eng. Des. **82**(5-14), 1327–1334 (2007).
[35]M. L. Reinke, "Experimental tests of parallel impurity transport theory in tokamak plasmas," Ph.D. dissertation (Massachusetts Institute of Technology, 2011); Available Online: http://www.psfc.mit.edu/library1/catalog/reports/2010/11rr/11rr014/11rr014_abs.html
[36]F. Penzel, H. Meister, M. Bernert, T. Sehmer, T. Trautmann, M. Kannamüller, J. Koll, and A. W. Koch, "Automated *in situ* line of sight calibration of ASDEX Upgrade bolometers," Fusion Eng. Des. **89**(9-10), 2262–2267 (2014).
[37]N. R. Walkden, J. Harrison, S. A. Silburn, T. Farley, S. S. Henderson, A. Kirk, F. Militello, and A. J. Thornton, "Quiescence near the X-point of MAST measured by high speed visible imaging," Nucl. Fusion **57**(12), 126028 (2017).
[38]L. L. Lao, H. St. John, R. D. Stambaugh, A. G. Kellman, and W. Pfeiffer, "Reconstruction of current profile parameters and plasma shapes in tokamaks," Nucl. Fusion **25**(11), 1611–1622 (1985).
[39]W. Morris, J. R. Harrison, A. Kirk, B. Lipschultz, F. Militello, D. Moulton, and N. R. Walkden, "MAST Upgrade divertor facility: A test bed for novel divertor solutions," IEEE Trans. Plasma Sci. **46**(5), 1217–1226 (2018).
[40]M. Bernert, F. Janky, B. Sieglin, A. Kallenbach, B. Lipschultz, F. Reimold, M. Wischmeier, M. Cavedon, P. David, M. G. Dunne, M. Griener, O. Kudlacek, R. M. McDermott, W. Treutterer, E. Wolfrum, D. Brida, O. Février, S. Henderson, and M. Komm, "X-point radiation, its control and an ELM suppressed radiating regime at the ASDEX Upgrade tokamak," Nucl. Fusion **61**(2), 024001 (2021).
[41]A. Kallenbach, M. Bernert, M. Beurskens, L. Casali, M. G. Dunne, T. Eich, L. Giannone, A. Herrmann, M. Maraschek, S. Potzel, F. Reimold, V. Rohde, J. Schweinzer, E. Viezzer, and M. Wischmeier, "Partial detachment of high power discharges in ASDEX Upgrade," Nucl. Fusion **55**(5), 053026 (2015).
[42]B. Lipschultz, B. LaBombard, E. S. Marmar, M. M. Pickrell, J. L. Terry, R. Watterson, and S. M. Wolfe, "Marfe: An edge plasma phenomenon," Nucl. Fusion **24**(8), 977–988 (1984).
[43]S. N. Pandya, B. J. Peterson, M. Kobayashi, S. P. Pandya, K. Mukai, and R. Sano, "A reconsideration of the noise equivalent power and the data analysis procedure for the infrared imaging video bolometers," Rev. Sci. Instrum. **85**(12), 123501 (2014).
[44]M. Greenwald, "Density limits in toroidal plasmas," Plasma Phys. Controlled Fusion **44**(8), R27 (2002).
[45]L. C. Ingesson, "Comparison of methods to determine the total radiated power in JET," JET Joint Undertaking, Abingdon, Technical Report No. 99, 2000.